



A Non-parametric Discrete Fracture Network Model

Santiago Gómez¹ · José A. Sanchidrián¹ · Pablo Segarra¹ · Maurizio Bernardini¹

Received: 28 July 2022 / Accepted: 8 December 2022 / Published online: 25 January 2023
© The Author(s) 2023

Abstract

A discrete fracture network (DFN) model based on non-parametric kernel density estimators (KDE) and directional-linear statistics is developed. The model provides a characterization of the fracture network with distributions of fracture orientation and size jointly. A solution to the Bertrand paradox is used for the calculation of disk sizes from trace lengths, the latter calculated from the intersection of disks and highwall faces by triangulation. A Poisson point process is applied for the generation of the model, with fractures assumed to be flat and circular in shape, the number of fractures per unit volume (P_{30}) adjusted to match the experimental length of fractures per unit area (P_{21}). Length censoring of traces due to the surface dimension is considered in the calculations by including semi-bounded traces, i.e., traces censored in one of their ends. Orientation and size biases are corrected with a weighting function in the random sampling. The truncation effect whereby no traces shorter than some cut-off length are recorded, is addressed by a randomized optimization algorithm. The joint fracture orientation-size distribution model developed is tested with trace maps of discontinuities measured from photogrammetric models of twelve highwall faces of quarry benches, with outstanding results. Computational advantages over traditional parametric fracture models are addressed.

Highlights

- Nonparametric directional-linear statistics has been used for the construction of DFN models. The mathematical analysis of this new approach is described in detail.
- A new link between distributions of disc size and pseudo-trace lengths is established. Relationships between means and variances for the distributions of trace length and disc size are discussed.
- Censoring bias is corrected by a mixed random variable and truncation bias is corrected by including semibounded traces and using a probabilistic filter.
- The nonparametric DFN model developed is applied to photogrammetric discontinuity data maps. Consistency of the results is assessed and thoroughly discussed.

Keywords Rock mass characterization · Directional-linear kernel estimator · Fracture density · Bertrand paradox · Trace length · Discontinuity censoring and truncation

List of Symbols

α	Scale parameter of the probabilistic filter (m)	δ	Angle derived from the von Mises kernel smoother (rad)
β	Sensitivity of the probabilistic filter	ϵ	Algorithm stop criterion
γ	Ratio between the histogram of disk sizes that intersect the surface and the histogram of true disk sizes	η	Arbitrary argument
		θ	Dip direction of a disk (rad)
		$\hat{\kappa}$	Maximum likelihood estimator of the concentration parameter
		Λ	Radial distance of the randomly selected point on the reference radius random variable (m)
		μ^T	Mean normal vector of the outcrop (m)
		Ξ	Mixed random variable
		ξ	Support of the random variable Ξ

✉ José A. Sanchidrián
ja.sanchidrian@upm.es

¹ Universidad Politécnica de Madrid—ETSI Minas y Energía, Ríos Rosas 21, 28003 Madrid, Spain

Ψ	Product distribution of Y by Ξ	OP	Parametrization of the hemisphere–cone intersection (m).
ψ	Support of the random variable Ψ	P	Probability
Ω_q	Support of the directional random variable	p	Ratio of semi-bounded traces over the total number of traces
ω_q	Lebesgue measure in Ω_q	\mathcal{G}	Cumulative distribution function of \mathcal{G}
A	Area of a single disk (m^2)	P_{30}	Intensity parameter, number of disk centers inside a volume (m^{-3})
A'	Projected area of a single disc (m^2)	\hat{P}_{30}	Estimator of P_{30} (m^{-3})
a	Constant of the size weighting function	P_{21}	Intensity parameter, length of fractures per unit area (m^{-1})
b	Constant of the orientation weighting function	P_{32}	Intensity parameter, total disk area divided by the volume of the domain (m^{-1})
c	Center of the shifted cone (m)	q	Dimension of the sphere
$c_{h,q}$	Normalizing constant	R	Disk radii random variable (m)
\mathcal{D}	Disk size random variable (m)	r	Radius (m)
D	Disk size (m)	t	Random angle between 0 and 2π (rad)
$\hat{F}_{\mathcal{D}}$	Cumulative distribution function of disk size for a single orientation	TF	Total number of fractures generated in the domain
\hat{F}_{\uparrow}	Cumulative distribution function of incomplete pseudo-trace length for a single orientation	\mathbf{u}	Horizontal vector (m)
$\hat{f}_{\mathcal{D}}$	Probability density function of disk size for a single orientation	V	Volume of the domain (m^3)
f_g	Probability density function of sizes	\mathbf{v}	Cross product of \mathbf{n} by \mathbf{u} (m)
\hat{f}_g	Kernel density estimator (KDE) of sizes	v_D	Standard deviation of diameters of the discontinuities generated in the domain (m)
\hat{f}_h	Probability density function of orientations	v_L	Standard deviation of trace lengths of the discontinuities that intersect a planar surface (m)
\hat{f}_h	KDE of orientations	w	Weighting function
$\hat{f}_{h,g}$	Joint probability density functions of orientation-sizes	X	Directional random variable (m)
$\hat{f}_{h,g}$	Joint KDE of orientation-sizes	X_i	Sample of the directional random variable (m)
f_W	Weighted probability density function	\mathbf{x}	Orientation (m)
f_Z	Any probability density function of sizes	Y	Ratio between \mathcal{L} and \mathcal{D}
f_{Z^*}	Log-transformed probability density function	y	Support of the random variable Y
g	Linear bandwidth	Z	Linear random variable (m)
g_{mlcv}	Maximum likelihood cross-validation linear bandwidth selector	Z_i	Sample of the linear random variable (m)
h	Directional bandwidth	z	Support of the linear random variable (m)
h_{ROT}	Rule-of-thumb directional bandwidth selector		
K_L	Directional kernel smoother		
K_Z	Linear kernel smoother		
\mathcal{L}	Complete pseudo-trace length random variable (m)		
L	Complete pseudo-trace length (m)		
\uparrow	Incomplete pseudo-trace length random variable (m)		
l	Incomplete pseudo-trace length (m)		
l_i	Experimental incomplete pseudo-trace lengths (m)		
\bar{l}	Mean of the experimental KDE of incomplete pseudo-trace lengths (m)		
\mathcal{G}	Log-transformed KDE of the linear part with Gaussian smoother		
m_D	Mean diameter of the discontinuities generated in the domain (m)		
m_L	Mean trace length of the discontinuities that intersect a planar surface (m)		
N	Total number of disks that intersect the surface (after filtering)		
\mathbf{n}	Pole of a disk in the lower hemisphere (m)		

1 Introduction

Characterization of fractured rock mass is a critical task in the development of open-pit and underground mining for the design of slopes, support means or blast optimization. Discrete Fracture Networks (DFNs) have proved to be an effective tool for the three-dimensional representation of a natural fracture network (Baecher et al. 1977; Long et al. 1982; Baecher 1983; Andersson et al. 1984; Dershowitz and Einstein 1988; Zhang et al. 2002; Miyoshi et al. 2018) and are increasingly being used in many geotechnical and mining engineering problems (Elmo et al. 2015; Elmouttie and Poropat 2012; Umili et al. 2020) e.g., in analysis of rock slope stability (Bonilla-Sierra et al. 2015), geo-mechanical and hydrological behavior of fractured rocks (Robinson 1983; Andersson et al. 1984; Lei et al. 2017), seismic attenuation and stiffness modulus dispersion Hunziker et al.

(2018), and multi-physics processes, see e.g., Keilegavlen et al. (2021).

The basis of the DFN method is the characterization of fracture parameters using statistical analysis to build a computational model that explicitly represents the geometrical properties of each individual discontinuity and the topological relationships between individual discontinuities and discontinuity sets (Lei et al. 2017; Miyoshi et al. 2018). In general, the term ‘discontinuity’ groups all weak planes of geological origin, such as fractures, joints, bedding planes, cleavages and faults (Lu 1997). In what follows we are treating all these terms equivalently. Among the geometrical properties of each fracture, one may emphasize orientation, size, location, shape and aperture and their corresponding probability distributions (Baecher et al. 1977; ISRM 1978; Baecher 1983; Dershowitz and Einstein 1988; Dershowitz and Herda 1992). Other relevant characteristics may also be considered, such as genetic type, filling material (Hekmatnejad et al. 2018) and roughness (Tang et al. 2022 and Zou et al. 2022).

Traditionally, DFN models group visible fractures by orientation in families of poles (ISRM 1978) on the stereographic projection. This is done by dividing the stereogram into sectors and fitting directional probability distributions. The most frequent are the bivariate von Mises–Fisher and Bingham (Bingham 1964; Baecher 1983; Fisher et al. 1993). The goodness of the fit is assessed using the chi-squared and the Kolmogorov–Smirnov tests (Baecher 1983). Similarly, analytical probability density functions (pdfs), such as log-normal, uniform, power law, gamma, normal, etc., are used to characterize the distribution of trace lengths measured on an outcrop (Tonon and Chen 2007). Even though analytical forms seldom provide satisfactory approximations to orientation data (Baecher 1983), works in which the statistical analysis is performed in a non-parametric way are rare, see e.g., Xu and Dowd (2010), and those that treat jointly the disk orientation and size pdfs in a non-parametric way are non-existent, to the authors’ knowledge. In this work, we use directional-linear statistics as a way to jointly estimate the density functions of fracture sizes and orientations, based on the theory of directional-linear kernels by García-Portugués et al. (2013). In directional statistics, the sample space is the unit sphere, while in directional-linear statistics, the sample space is the Cartesian product of a sphere and the real line.

Because the rock mass structure is impossible to be directly observed without dismantling it completely (Priest 1993), a variety of methods must be used for sampling discontinuity data. From that observation, the ‘true’ joint density function of orientation-sizes inherent to the rock mass is inferred through stereology. Data from exposed rock faces, such as natural outcrops, excavation faces, and boreholes have proved to be useful (Tonon and Chen 2007). Among sampling techniques for deriving fracture parameters, the

most utilized are in-hole images or wireline geophysical logging (Ozkaya and Mattner 2003; Hekmatnejad et al. 2019), scanline survey, circle sampling or window survey (Priest and Hudson 1981a, b; Kulatilake et al. 2003; Kulatilake and Wu 1984; Zhang and Einstein 1998, 2000; Song and Lee 2001; Jimenez-Rodriguez and Sitar 2006), as well as digital photogrammetry and laser scanning techniques (Elmo et al. 2015; Vollgger and Cruden 2016).

The history of the problem of determining density functions of disk sizes from trace length probability density functions is well summarized by Tonon and Chen (2007). The work of Warburton (1980b) provided a starting point for estimating trace length probability density functions from disk size density functions, using stereological principles, for disks without aperture, circular in shape, parallel to each other and with centers arranged within a volume following a Poisson process, see e.g., Baecher et al. (1977). Other contributions assume fractures to be elliptical in shape (Zhang et al. 2002) (Guo et al. 2022 and Zheng et al. 2022). The inverse process, i.e., obtaining disk sizes pdf from trace lengths, was already formulated years before by Santaló (1955). However, works by Tonon and Chen (2007, 2010) showed that this relationship leads in some cases to non-positive pdf values; it also fails for bimodal or multimodal distributions. As this type of distributions is common in the field, a solution to this problem is explored in this work using one of the Bertrand’s paradoxes (Bertrand 1888; Aldous et al. 1988; Chiu and Larson 2009) and its relation with Warburton’s work (Warburton 1980a).

When characterizing rock exposures, one should consider bias effects inherent to the sampling procedure. According to Kulatilake and Wu (1984), Priest and Hudson (1981a, b), Laslett (1982), Baecher and Lanney (1978), Baecher (1983), Villaescusa and Brown (1992) and Chilès and Marsily (1993) there are four main causes of bias in the distribution of trace lengths: censoring, truncation, size and relative orientation. Censoring occurs when one or both terminations of a trace are not observable. This effect occurs when the surveying surface is finite; the disk orientation-size density function and the size, shape and orientation of the surface to be intersected have also some influence. The resulting traces may be grouped into three categories according to the number of terminations or censoring condition, namely complete, semi-bounded and bounded (White and Willis 2000). Truncation is introduced because traces shorter than a cut-off length (Baecher 1983) cannot be observed. When an observer maps traces on an outcrop, unintentional truncation occurs. Operator’s skills, and sampling scale, makes that small traces are less likely to be observed. That is what Riley (2005) called ‘the protocol adopted for recording short traces (lower truncation limit)’. Size bias occurs because longer traces are more likely to be sampled than shorter

ones (Baecher 1983; Jimenez-Rodriguez and Sitar 2006) thus, large fractures are over-represented and this must be considered when estimating the true size distribution. A fourth bias effect is caused by the relative orientation between fractures and the outcrop surface: a fracture is more likely to intersect a surface the more perpendicular their relative orientations are. All these phenomena need to be suitably accounted by the model to interpret the true nature of the rock mass in the best possible way.

The spatial structure of the fractures' support points is another fundamental aspect in DFN models. The homogeneous Poisson-Boolean point process has been widely used (Baecher et al. 1977; Kulatilake and Wu 1984; Zhang and Einstein 1998; Song and Lee 2001; Jimenez-Rodriguez and Sitar 2006; Hekmatnejad et al. 2019). Other types of point-supporting processes are the doubly stochastic Poisson, or Cox, the Levy–Lee Fractal, the non-stationary Poisson and the Gibbs processes, among others. See e.g., Aldous et al. (1988), Lee et al. (2011) and Hekmatnejad et al. (2019). The decision on the process to be applied depends on the overall breakage pattern of the rock.

In this work, a novel distribution-free DFN generation technique is developed. It uses a directional-linear KDE to characterize the joint distribution of orientations and trace lengths in a non-parametrical way. The DFN models are calibrated using Monte Carlo realizations of the non-parametric distributions (Zheng et al. 2014 and Zheng et al. 2015). Poisson point process is used for fractures location and these are assumed to be flat and circular in shape. Triangulated surfaces are used to conduct the intersection of a disk with a three-dimensional surface; a MATLAB (MATLAB 2019) function called `SurfaceIntersection.m` (Tuszynski 2014) based on a triangle/triangle intersection algorithm proposed by (Moller 1998) is used for this purpose. A solution to the Bertrand paradox (Bertrand 1888; Chiu and Larson 2009) is considered to estimate disk sizes from trace lengths. Correction of sampling biases is also addressed. The experimental value of P_{21} , i.e., length of fractures per unit area for each trace map, is fitted through the number of fractures per unit volume (P_{30}), see (Zheng et al. 2017). Field data used to test the model were collected from photogrammetric models of non-planar highwall faces. Disk orientations are obtained by fitting a plane to the 3D coordinates of the polyline fitted to the exposed trace.

In the following sections, data collection and subsequent data processing techniques are described; the mathematical foundations of the model are developed and the calibration process presented. The results obtained from the model are shown, followed by a discussion on the approximation to calculate the trace length distributions and its validity. The influence of the surface on the distribution of trace lengths and the relation between fracture intensities is also investigated.

2 Data Overview

The experimental work was carried out at El Aljibe quarry (Almonacid de Toledo, Spain), where mylonite is mined by drilling and blasting. Discontinuities were mapped from photogrammetric models of the highwall faces of 12 blasts in which the sampling scale was about 10 mm. The blasts were arranged in two test campaigns of six blasts each, located in the same area of the pit. A major extensional fault defines two structural domains DS1 (trace maps TM1–TM6) and DS2 (trace maps TM7–TM12) with different fracture density. Bernardini et al. (2022) give an insight to data collection, discontinuity sets and a classical DFN construction using the FracMan[®] suite (Golder Associates 2018).

For the analysis, point clouds of the outcrops and discontinuity characteristics (dip, dip direction, and coordinates of polylines' points) are treated in.csv format. The orientations of the 12 faces are similar with a dip direction of $228.54 \pm 4^\circ$ and a dip of $22.98 \pm 3.59^\circ$ (circular mean \pm standard deviation). Because the inspected area is smaller than the area of the complete photogrammetric model, it is cropped with a MATLAB function in a way that the parameter P_{21} is not affected. The limits of the outcrop surface considered for the calculations are defined by the minimum and maximum coordinates of the traces. The resulting surface areas range between 200 m² (TM6) and 390 m² (TM10) approximately.

The number and length of the mapped fractures are shown in Table 1. It also shows the sampling window dimensions, areal fracture density P_{21} and the percentage of complete, semi-bounded and bounded traces. These are plotted in red, green and blue, respectively in the trace maps of the twelve faces shown in Fig. 1; complete discontinuities correspond to more than 85% of the total, while bounded fractures are observed only in five blasts. Figure 16 shows the stereograms of the experimental poles obtained for each trace map (black dots). There is an increase in the number of fractures marked in DS2 domain (trace maps TM7–TM12), due likely to the effect of the fault mentioned above. This results in a mean P_{21} of 0.72 m⁻¹ for DS1 and 1.23 m⁻¹ for DS2. The histograms of the lengths of the fractures mapped are shown in Sect. 3.1.2 (Fig. 4).

3 Model Description

The DFN model proposed treats fractures individually instead of considering their belonging to a certain set or family. KDEs are suitable to this end, since they are versatile enough to be used in both directional and linear domains. A Poisson–Boolean point process has been considered to model the location of the support points which is characterized by a constant parameter, P_{30} . Disks are described as

Table 1 Main characteristics of mapped discontinuities

	Face dimensions (m) Height × width	Trace characteristics			$P_{21}(m^{-1})$	Trace type ^a (%)		
		No	Length (m)			C	S	B
			Total	Mean				
TM1	9.3 × 19.2	66	188.6	2.86	0.82	89.4	6.0	4.6
TM2	8.7 × 21.1	54	164.7	3.05	0.59	87.0	13.0	0.0
TM3	9.6 × 20.9	50	159.6	3.19	0.60	94.0	6.0	0.0
TM4	10.1 × 18.3	91	218.4	2.40	0.92	93.4	6.6	0.0
TM5	11.0 × 17.3	58	152.5	2.63	0.62	94.8	5.2	0.0
TM6	9.8 × 16.9	74	157.3	2.13	0.79	89.2	9.5	1.3
TM7	10.4 × 20.5	141	305.9	2.17	1.00	95.0	5.0	0.0
TM8	11.7 × 21.5	165	306.3	1.86	0.90	95.8	4.2	0.0
TM9	10.3 × 19.8	267	570.0	2.13	1.81	95.5	4.6	0.0
TM10	13.4 × 20.4	202	479.3	2.37	1.23	95.5	4.5	0.0
TM11	9.6 × 17.6	206	427.5	2.08	1.39	97.1	2.9	0.0
TM12	10.1 × 19.6	242	288.0	1.19	1.05	95.9	3.7	0.4

^aC refers to complete, S to semi-bounded and B to bounded traces

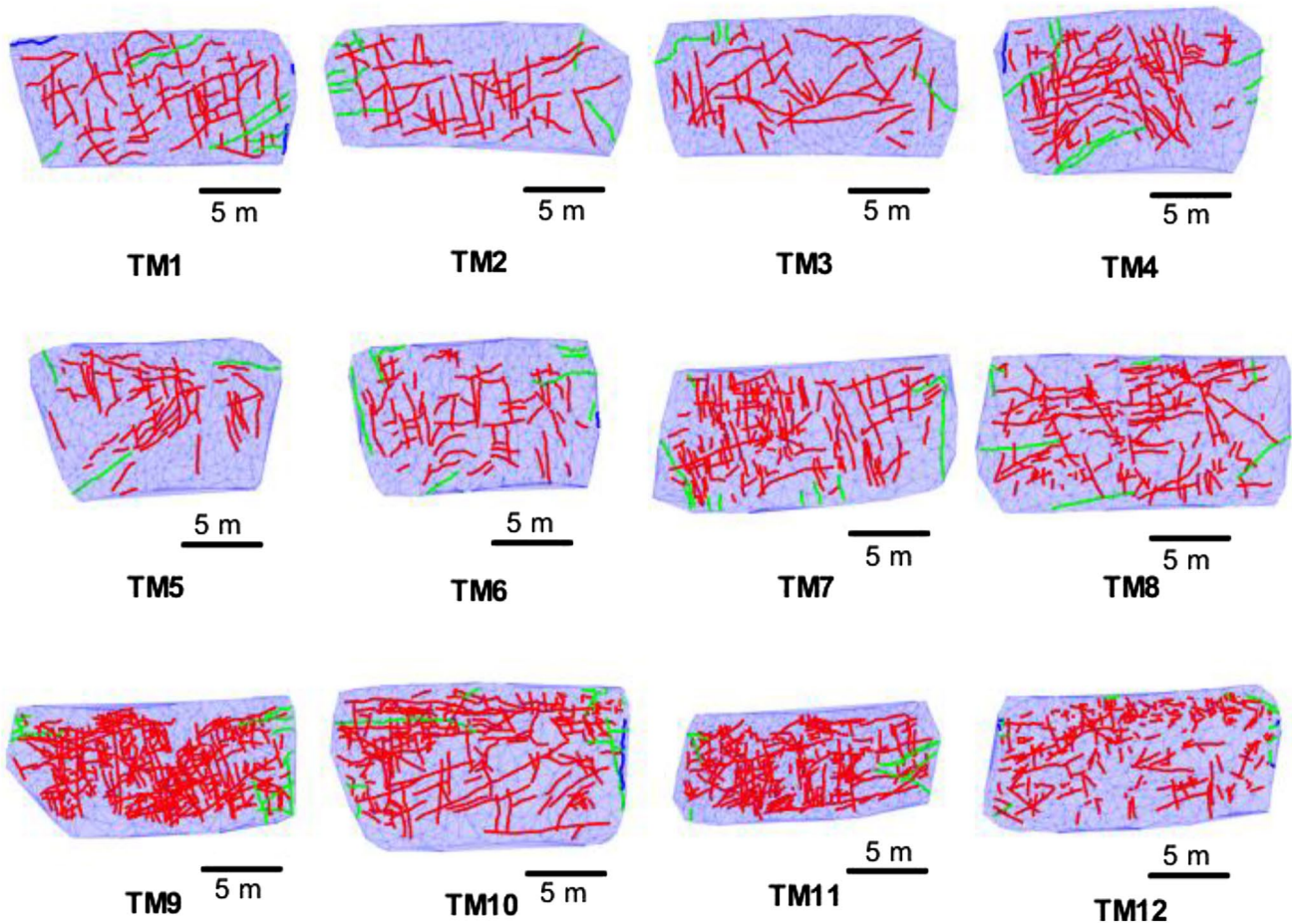


Fig. 1 Trace maps of the 12 benches analyzed. Different trace termination types are given with different colors: complete (red), semi-bounded (green) and bounded (blue) censored traces. Camera line of sight (azimuth, elevation) is (128°, 20°) (colour figure online)

flat and circular, although they are modeled as triacontagons.¹ Fracture sizes and orientations have been considered to be independent. Corrections are implemented to account for orientation, size, truncation and censoring biases and a method has been developed to random sampling the directional-linear KDE; this sampling method is also applicable to non-planar surfaces such as those observed in the field.

3.1 Directional-Linear Kernel to Represent Trace Maps

The DFN is based on a non-parametric distribution using the kernel density estimation for linear-directional data by García-Portugués et al. (2013).

Let Z denote a linear random variable with density f_g whose support is all the real numbers. For a random sample of Z , with size n , the traditional linear KDE is given by García-Portugués et al. (2013):

$$\hat{f}_g(z) = \frac{1}{ng} \sum_{i=1}^n K_Z\left(\frac{z - Z_i}{g}\right), z \in \mathbb{R} \tag{1}$$

where K_Z is a suitable kernel smoother, and g is the bandwidth of the linear part. In this work we assume a Gaussian smoother. This linear variable may be applied for any length or size of discontinuities equivalently. And let X denote a directional random variable in Cartesian coordinates with density f_h that accounts for orientation. The support of such a variable is the q -dimensional hemisphere, denoted by:

$$\omega_q = \omega_q(\Omega_q) = \frac{\pi^{\frac{q+1}{2}}}{\Gamma\left(\frac{q+1}{2}\right)}, q \geq 1 \tag{2}$$

where ω_q is the Lebesgue measure in Ω_q , which is the surface area of Ω_q and $\Gamma(\cdot)$ is the gamma function. For spherical data $q=2$ and the Lebesgue measure in Ω_2 is 2π . Likewise, for a random sample of X , the directional KDE is given by García-Portugués et al. (2013):

$$\hat{f}_h(x) = \frac{c_{h,q}(K_L)}{n} \sum_{i=1}^n K_L\left(\frac{1 - x^T X_i}{h^2}\right), x \in \Omega_q \tag{3}$$

where K_L is a suitable kernel smoother, h is the bandwidth of the directional part and $c_{h,q}(K_L)$ is a normalizing constant for any $x \in \Omega_q$, which is given by García-Portugués et al. (2013):

$$c_{h,q}(K_L)^{-1} = \int_{\Omega_q} K_L\left(\frac{1 - x^T y}{h^2}\right) \omega_q(dy) \sim h^q 2^{\frac{q}{2}-1} \omega_{q-1} \int_0^\infty K_L(\eta) \eta^{\frac{q}{2}-1} d\eta \tag{4}$$

In this case, the von Mises–Fisher kernel smoother has been chosen for simplicity:

$$K_L(\eta) = e^{-\eta} \tag{5}$$

For a directional-linear random variable (X, Z) with support $\Omega_q \times \mathbb{R}$ and joint density $f_{h,g}$, the KDE of orientation-sizes may be expressed as (García-Portugués et al. 2013):

$$\hat{f}_{h,g}(x, z) = \frac{c_{h,q}(K_L)}{ng} \sum_{i=1}^n K_L K_Z\left(\frac{1 - x^T X_i}{h^2}, \frac{z - Z_i}{g}\right), (x, z) \in \Omega_q \times \mathbb{R} \tag{6}$$

where the notation $K_L K_Z$ should be understood as:

$$K_L K_Z(a, b) = K_L(a) K_Z(b) \tag{7}$$

3.1.1 Log-transformed Kernel for Linear Data

To have a kernel support positive, to prevent negative sizes in the distribution, and to meet the condition $f_g(0) = 0$, a variable $Z^* = \ln(Z)$ is introduced (Geenens and Wang 2018). From standard arguments, one has:

$$f_Z(z) = \frac{f_{Z^*}(\ln z)}{z}, z > 0 \tag{8}$$

which readily suggests using the estimator \hat{f}_{Z^*} of f_{Z^*} .

$$\hat{f}_Z(z) = \frac{\hat{f}_{Z^*}(\ln z)}{z}, z > 0 \tag{9}$$

3.1.2 Optimal Bandwidths

Bandwidth selection of the KDE is an important aspect in non-parametric statistics; the rule-of-thumb (ROT) bandwidth selector h_{ROT} for directional data (García-Portugués et al. 2013) is considered in this work:

$$h_{ROT} = \left(\frac{8 \sinh^2(\hat{\kappa})}{n \hat{\kappa} [(1 + 4\hat{\kappa}^2) \sinh(2\hat{\kappa}) - 2\hat{\kappa} \cosh(2\hat{\kappa})]} \right)^{1/6} \tag{10}$$

The parameter $\hat{\kappa}$ is estimated by maximum-likelihood. The ROT selector is simple but fails when estimating directional densities with multimodality (García-Portugués 2013). This is an issue in geological discontinuity representation, since orientation measurements often present multimodality (in fact the usual procedure is to group

¹ Thirty-sided regular polygon.

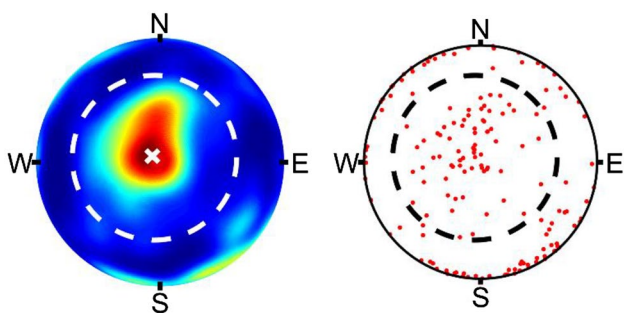


Fig. 2 Example of calculation of h_{ROT} . Marginal KDE of orientations (left) and experimental poles (right) for trace map TM8. Dashed lines are the intersection of a cone of 45° with the hemisphere

traces by families, i.e., different modes). To solve this, we consider only data around the likeliest point in the stereogram, so that the information of the main mode is well fitted. h_{ROT} is then calculated from points that do not differ more than 45° from the likeliest point. Figure 2 shows as example the likeliest orientation and the area considered to calculate h_{ROT} with Eq. (10) in trace map TM8; the marginal KDE of orientation plotted was obtained with $h_{ROT} = 0.126$. The location of points more than 45° away from the likeliest pole is obtained through a parametrization of the hemisphere–cone intersection (see Sect. 3.3.2).

The marginal KDEs of the discontinuity orientation are shown in Fig. 3. They are constructed onto a dense equi-spaced Fibonacci grid through a MATLAB algorithm called `SpiralSampleSphere.m` (Semechko 2012). The likeliest orientations, which are not evident in all the graphs, are marked with white crosses. Bandwidths from Eq. (10) are given in Table 4.

For the linear part of the KDE, the maximum-likelihood cross-validation MLCV (García-Portugués 2013) is used for bandwidth selection; g is chosen to maximize the following quantity:

$$g_{mlcv} = \underset{g>0}{\operatorname{argmax}} \operatorname{MLCV}(g) \tag{11}$$

where $\operatorname{MLCV}(g)$ is given by (García-Portugués 2013):

$$\operatorname{MLCV}(g) = \left(n^{-1} \sum_{i=1}^n \log \left[\sum_{j \neq i} K_Z \left(\frac{Z_j - Z_i}{g} \right) \right] - \log[(n-1)g] \right) \tag{12}$$

Figure 4 shows the histograms (blue bars) and the marginal KDEs (red lines) of pseudo-trace lengths (see next section) calculated with the bandwidths obtained with Eqs. (11) and (12). They are given in Table 3

3.2 Trace Length-to-Fracture Size Distribution Estimation

When a fracture, in this case modeled as a circular disk of a given size, intersects a plane surface of infinite extension, the result is a line whose initial and final points are located on the perimeter of the disk. The exposure of this intersection on the surface is called trace and its length is traditionally called trace length. However, when the surface is non-planar, the intersection between the disk and the surface becomes a polyline. Its length, if measured in 3D, is that we call the ‘true’ trace length. The higher the specific area of the surface, the longer the true length is. This is an inconvenience when calculating fracturing intensity parameters that must be matched with experimental measures since these are closer to the projected length on the mean plane of the surface. This is solved by considering the pseudo-trace length of the chord that a disk forms when intersects the irregular three-dimensional surface.

The probability of a trace obtained from the intersection of a disk with a surface of infinite extension to have a certain length can be approached with the Bertrand’s Paradox (Bertrand 1888). This, however, offers several answers, all plausible, to the interpretation of the concept of randomness Chiu and Larson (2009). Intuitively, one might choose the paradox No. 3, in which the chord center is assumed to be uniformly distributed over a reference radius. This is equivalent to selecting a random point on a reference radius to become the center of a random chord (see Fig. 5).

Following the scheme in Fig. 5, if one starts from the basis of a disk size distribution \mathcal{D} , or a disk radii distribution $R = \mathcal{D}/2$ (a triangular distribution has been chosen arbitrarily for the distribution of radii in the right graphs of Fig. 5), and takes any point on a reference radius of any of those disks, a distribution of lengths Λ from the center of the disk to the mentioned point can be formed. For an arbitrary disk radius r , Λ can take values between 0 and r following a uniform distribution, then Λ may be written as the product of two distributions:

$$\Lambda = R \cdot U(0, 1) \tag{13}$$

where $U(0,1)$ is the uniform distribution between 0 and 1. Equation (14) is represented as operation a on the right part of Fig. 5. From Fig. 5, the distributions of \mathcal{L} , R and Λ are related by:

$$\mathcal{L} = 2\sqrt{R^2 - \Lambda^2} \tag{14}$$

Inserting Eq. (13) in Eq. (14), \mathcal{L} may be directly obtained from \mathcal{D} :

$$\mathcal{L} = \mathcal{D}\sqrt{1 - U^2(0, 1)} \tag{15}$$

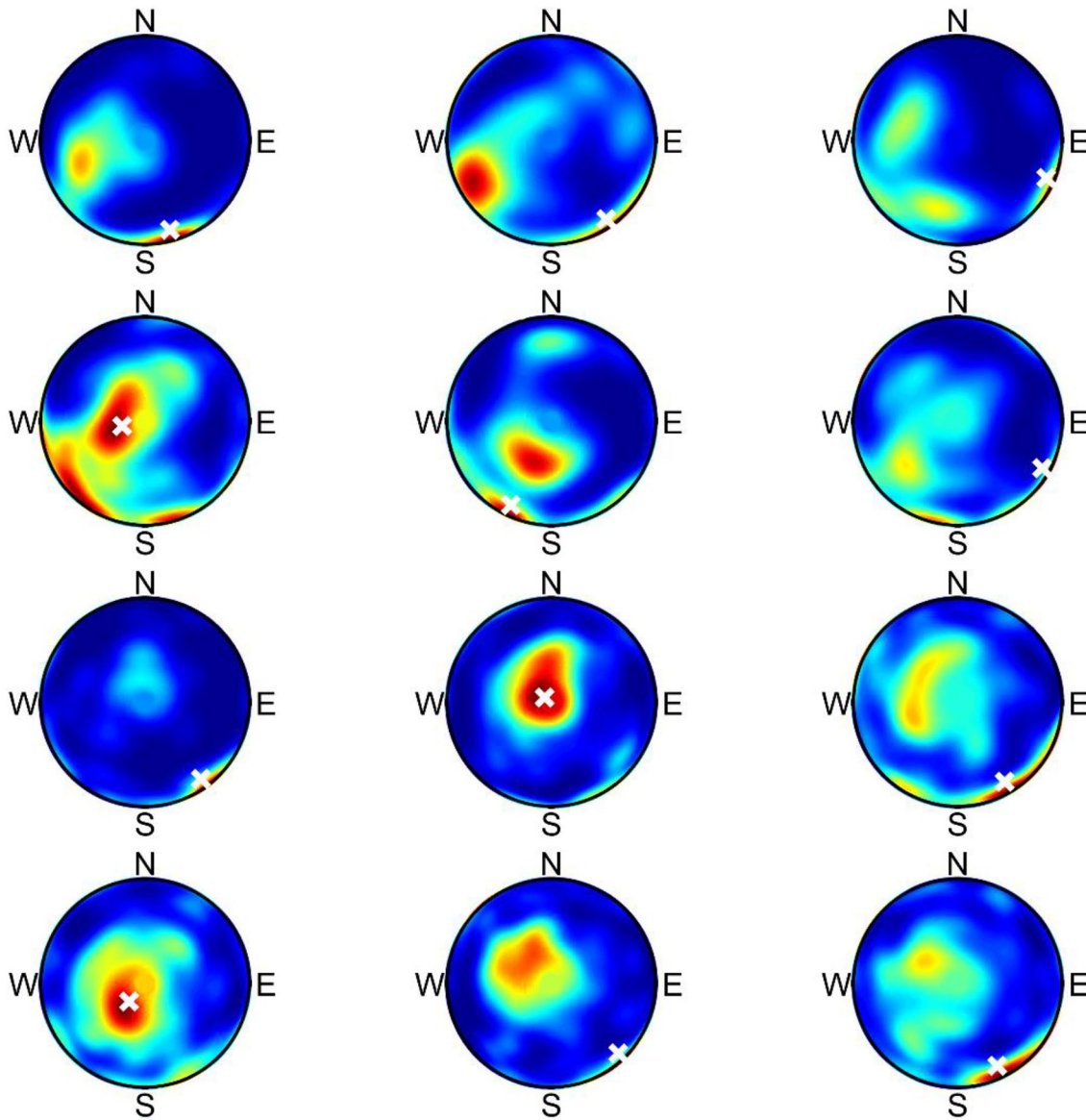


Fig. 3 Marginal KDE of orientations and likeliest points in the stereogram (white crosses) for each highwall face; data is sorted horizontally from top left to bottom right (colour figure online)

Equation (15) is equivalent to the Warburton's relationship for estimating trace length probability density, as shown in Appendix A.1, see Eqs. (39–42). Appendix A.2 demonstrates that Eq. (15) is consistent with Bertrand's paradox No. 3. Equation (15) is represented on the right part of Fig. 5, operation b.

Dividing the pseudo-trace lengths by their respective diameters one may obtain:

$$\frac{\mathcal{L}}{D} = Y \quad (16)$$

where Y is a random variable whose density function may be expressed as:

$$f_Y(y) = \frac{y}{\sqrt{1-y^2}}, \quad y \in [0, 1] \quad (17)$$

A proof of the validity of Eq. (17) is offered in Appendix A.3.

In practice, the outcrop has finite extension so that some traces are censored. Thus, a modification that corrects the censoring bias has to be included. This is accomplished with a mixed random variable \mathcal{E} :

$$\uparrow = D \cdot \Psi \quad (18)$$

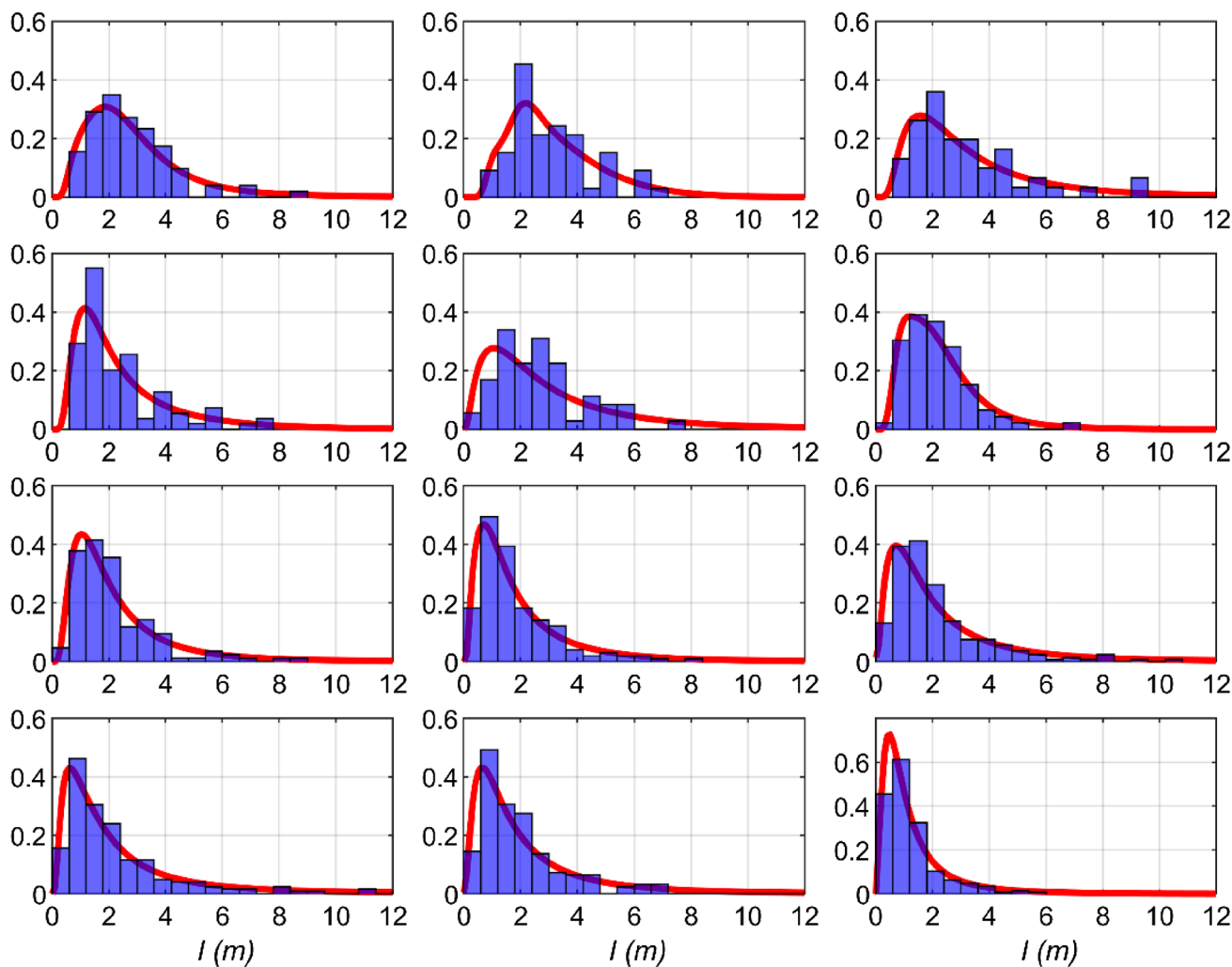


Fig. 4 Marginal KDE of trace lengths for each highwall face. Experimental data (histograms) and KDEs (red lines); data is sorted from top left to bottom right (colour figure online)

where \uparrow is the incomplete pseudo-trace length random variable, see Fig. 5 operation d, and Ψ a new random variable resulting from multiplying Y and Ξ , see Fig. 5 operation c, using the properties of product distributions. The following cumulative distribution function has been selected for Ξ :

$$F_{\Xi}(\xi) = \begin{cases} p\xi^2, & 0 \leq \xi < 1 \\ 1, & \xi \geq 1 \end{cases} \tag{19}$$

where p is a parameter that indicates the proportion of semi-bounded traces over the total number of traces; it is one of the fitting parameters of the model. This function has been built to be a mixed random variable so that it only applies to a proportion of fractures to be treated as semi-bounded; the square has been chosen to enhance the occurrence of long traces. The resulting probability density function of Ψ is:

$$f_{\Psi}(\psi) = -p\psi(\sqrt{1-\psi^2}-1) \left(\frac{\psi^2}{\sqrt{1-\psi^2}(\sqrt{1-\psi^2}+1)^2} + \frac{1}{\sqrt{1-\psi^2}+1} \right) - 2p\psi \ln\left(\frac{\psi}{\sqrt{1-\psi^2}+1}\right) + \frac{\psi}{\sqrt{1-\psi^2}}, \psi \in [0, 1] \tag{20}$$

A proof of the validity of Eq. (20) is offered in Appendix A.4.

Equation (18) is of key importance, as it directly relates trace lengths with their respective disk sizes including the censoring bias; moreover, it allows using non-analytic

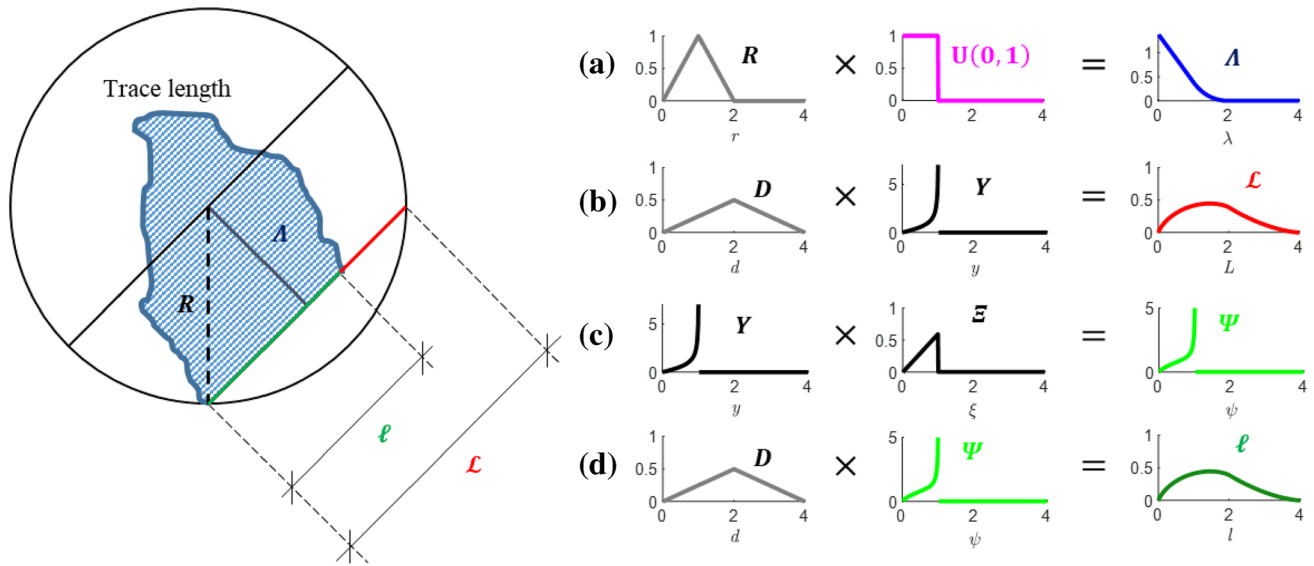


Fig. 5 Scheme for calculation of the pseudo-trace length distribution from a disk size distribution. $D=2R$ disk diameter; A radial distance to the center of the chord; \uparrow incomplete pseudo-trace length; \mathcal{L} com-

plete pseudo-trace length. The functions and their operations represented on the right of the figure relate to Eqs. (13–20)

distributions and finite surfaces to obtain the disk size distribution for each orientation, based on the distribution of measurable trace lengths using the definition of ratio distribution:

$$\hat{f}_D(\mathbf{X}_i, D) = \int_0^1 \psi f_\psi(\psi) \frac{\hat{f}_{h,g}(\mathbf{X}_i, D\psi)}{\int_0^\infty \hat{f}_{h,g}(\mathbf{X}_i, l) dl} d\psi \quad (21)$$

where the KDE $\hat{f}_{h,g}$ is used. A list of quadruplets composed by the Cartesian coordinates of each pole on the unit hemisphere, and the incomplete pseudo-trace lengths, is associated to each trace map. For a given orientation \mathbf{X}_i (the first three) there is a one-dimensional function of the type $\hat{f}_{h,g}(\mathbf{X}_i, l)$ (see the integrand in Eq. (21)). Such function is normalized to obtain the cumulative distribution function \hat{F}_{\uparrow} . This may be done for each \mathbf{X}_i so that a disk size distribution is obtained for each orientation. To obtain disks larger than the incomplete pseudo-trace length with which it is associated, the distribution function of experimental incomplete pseudo-trace lengths is used to calculate the probability level of a given pseudo-trace l_i . This level is considered in the distribution function obtained from Eq. (21) to get the respective disk size D_i through:

$$\hat{F}_D(\mathbf{X}_i, D_i) = \hat{F}_{\uparrow}(\mathbf{X}_i, l_i) \quad (22)$$

where \hat{F}_D is the distribution function obtained from Eq. (21).

To simplify the calculation, these functions are taken as piecewise linear. Equation (21) is solved numerically for each pseudo-trace. Figure 6 shows the result for trace map TM12 and $P=0.18$. As it should, the cumulative distribution

of disk sizes (in red) is shifted to the right, so that chord length percentiles are always smaller than the percentiles of fracture size.

3.3 KDE Random Sampling

To construct a DFN model, the directional-linear kernel must be sampled randomly. This is done by (i) random sampling the kernel smoother, (ii) randomly selecting one of the experimental data points with replacement and (iii) adding both values. Random sampling must consider that each point has a different weight, as will be explained in Sect. 3.3.3. The properties of the kernel are associated to all points that

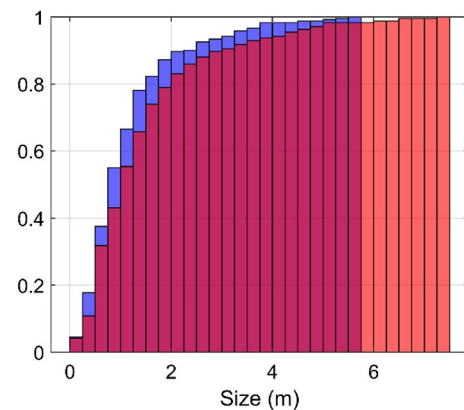


Fig. 6 Disk size distribution (red) for trace map TM12 from the experimental pseudo-trace length distribution (blue) (colour figure online)

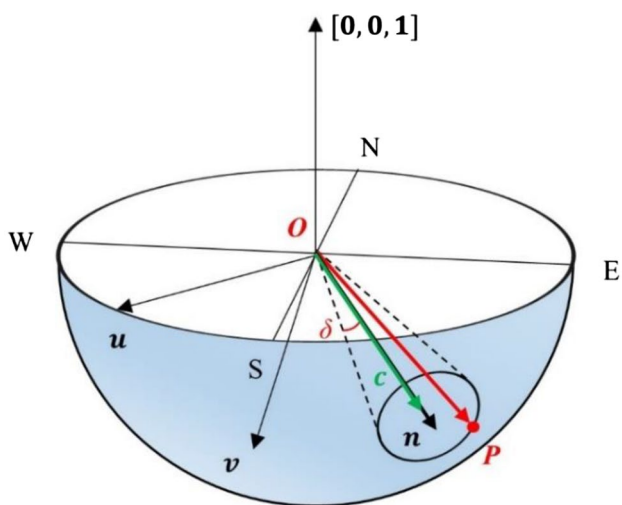


Fig. 7 Random sampling of orientations

make up the support. As a Poisson–Boolean point process, it is characterized by two fundamental properties: (i) Poisson distribution of point counts and (ii) completely random position in the bounded region (Aldous et al. 1988).

3.3.1 Random Sampling of Disk Sizes

Once KDE is sampled, the disk size is taken from the quadruplet associated to each individual discontinuity. A random value depending on the kernel smoother used and the directional bandwidth must be added or subtracted to the disk size. For convenience, it is possible to transform the linear kernel into a quantile function; let be the linear part of the KDE:

$$\mathfrak{Z}(z, Z_i; h) = \frac{1}{zg} K_Z \left(\frac{\ln z - \ln Z_i}{g} \right) \tag{23}$$

Since a Gaussian smoother is used, the cumulative distribution function of \mathfrak{Z} is given by:

$$\wp = \frac{1}{2} + \frac{1}{2} \operatorname{erf} \left(\frac{\ln z - \ln Z_i}{g\sqrt{2}} \right) \tag{24}$$

where erf is the error function. Solving for z in Eq. (24), one obtains:

$$\ln z = \ln Z_i + g\sqrt{2} \operatorname{erf}^{-1}(2\wp - 1) \tag{25}$$

3.3.2 Random Sampling of Orientations

For the purpose of randomly sampling orientations on the unit hemisphere, points within a certain angular distance around a pole must be selected. This may be accomplished

by intersecting a cone with a random opening angle with the hemisphere and then randomly selecting one of the points on the intersection circle. This way, a parametrization of the circle $(\sin\delta\cos t, \sin\delta\sin t)$ is carried out by mapping it onto the cone-hemisphere intersection; δ is the cone’s half angle and t a random angle between 0 and 2π . The transformation consists of a rotation and a translation, which reduces to finding a suitable orthonormal basis for \mathbb{R}^3 . Figure 7 illustrates the orientation sampling process.

For the translation part, the center of the circle is shifted from the origin to:

$$c = \cos\delta n \tag{26}$$

where c is the intersection of the cone’s axis with the circle’s plane and n is a unit vector which corresponds to the Cartesian coordinates of any disc’s pole. For the rotation part, the z -axis must be mapped to the normal of the intersection circle’s plane. If:

$$n = (n_x, n_y, n_z)^T \tag{27}$$

Then let

$$u = \frac{n \times (0, 0, 1)^T}{\|n \times (0, 0, 1)^T\|} \tag{28}$$

be a horizontal unit vector and

$$v = n \times u \tag{29}$$

With these two vectors, one may construct the parametrization:

$$OP = c + \sin\delta\cos tu + \sin\delta\sin tv \tag{30}$$

δ is derived from the von Mises kernel as a quantile function:

$$\cos\delta = h^2 \ln \left\{ \wp \left(e^{2/h^2} - 1 \right) + 1 \right\} - 1, \wp \in [0, 1] \tag{31}$$

If the z coordinate of P is positive, then it is transformed in its antipode, so that it is always on the lower hemisphere.

3.3.3 Weighting Function for Random Sampling

When sampling a joint distribution of disk orientations-sizes within a domain and intersecting them with the highwall face, a disk is more likely to intersect the surface the larger and the closer to perpendicular to the surface it is. Three joint orientation-size distributions are considered: (i) the ‘true’ distribution, (ii) the distribution of disks that intersect the surface, and (iii) the experimental distribution of pseudo-traces. Weighting must be applied to both size and orientation to obtain (i) from (ii), and vice versa. Obtaining

Fig. 8 Example of calculation of γ . Green and red histograms in the left graph represent the ‘true’ distribution of disks and the distribution of disks that intersect the surface, respectively (colour figure online)

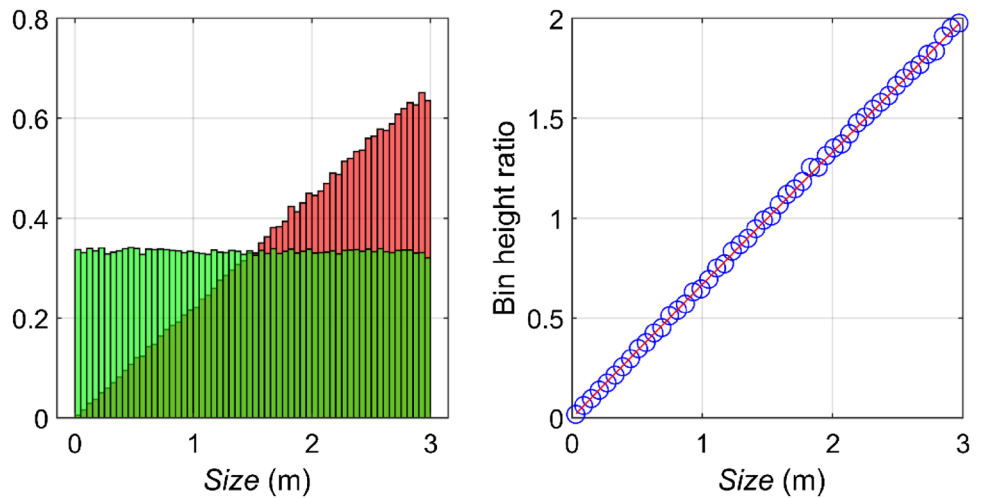
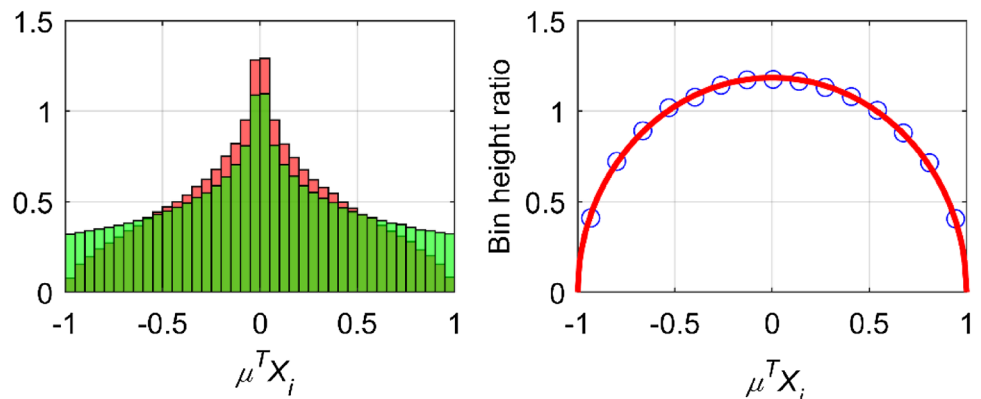


Fig. 9 Weighting function for orientations. Green and red histograms in the left graph represent the ‘true’ distribution of the dot product $\mu^T X_i$ and the distribution of disks that intersect the surface, respectively (colour figure online)



a weighted density function from another is accomplished through the following relation (Saghir et al. 2017):

$$f_w(z) = f(z) \frac{w(z)}{E[w(Z)]} \tag{32}$$

where $w(x)$ is an appropriate weighting function and $E[\cdot]$ denotes mathematical expectation. Here $f(z)$ and $f_w(z)$ correspond to distributions (i) and (ii), respectively. Equation (32) may be applied for sizes and orientations equally. $w(z)$ may be numerically obtained by computing the ratio between the bin values of the histogram of sizes of disks that intersect the surface (distribution ii) and the histogram of sizes of all the disks generated within the domain (distribution i). These ratios fit well a power law:

$$w(z) = az^\gamma \tag{33}$$

a being a constant and γ an additional fitting parameter of the model. The value of a is not relevant because it vanishes when normalizing. Baecher (1983) already considered a quadratic weighting function.

Figure 8 shows the process of obtaining γ . By way of example, five hundred thousand disks that follow a uniform distribution of diameters between 0 and 3 m and with random orientation are modeled. Green and red histograms in the left graph represent the ‘true’ distribution and the distribution of disks that intersect the surface, respectively. Note the size bias effect caused by the surface. The ratio between bin values of both histograms is shown in the right graph (blue circles). The determination coefficient of fitting Eq. (33) to these points (red line) is 0.996, $a = 0.6675 \pm 4.7 \cdot 10^{-3}$ and $\gamma = 0.9959 \pm 8.3 \cdot 10^{-3}$ at confidence level of 95%. The fact that an infinite planar surface is assumed makes $\gamma \approx 1$. For a non-planar case, γ takes values higher than 1. For the faces studied in this work, γ ranges from 1.13 to 1.48 (see Table 4 in Appendix B); γ is statistically significant in all cases.

The bias correction due to the relative orientation between disks and the intersection surface (the classic Terzaghi correction (Terzaghi 1965) is made by the function:

$$w_i = b \sqrt{1 - (\mu^T X_i)^2} \tag{34}$$

where b is a constant and μ^T is the average normal vector to the surface in case this is non-planar. The value of b is not relevant because it vanishes when normalizing. The `vertexNormal.m` function in MATLAB has been used to calculate μ^T which is the normal unit vector to the surface at each of the points of the face. This is a modified version from Mauldon and Xiaohai (2006).

Figure 9 shows the validity of Eq. (34) for a similar simulation, including an infinite planar surface, to that in Fig. 8. The true density function of the dot product $\mu^T X_i$ is the green histogram in the left graph, and the red one is the distribution of disks that intersect the surface. The ratio between bin values of both histograms is shown in the right graph (blue circles). Fitting Eq. (34) (red line) to these points leads to a determination coefficient of 0.9984 with $b = 1.186 \pm 7 \cdot 10^{-3}$ at a confidence level 95%.

Equations (33) and (34) are combined into a single weighting function for calculating the true distribution from the distribution of disks that intersect the surface:

$$w_i = \left(1 - (\mu^T X_i)^2\right)^{-1/2} Z_i^{-\gamma} \tag{35}$$

3.4 Probabilistic Truncation

Truncation can be described as a ‘perfect filter’ that discards samples when a certain bound is exceeded. This work considers a ‘probabilistic filter’ that groups the sources of error cited in Sect. 1 above and truncates fractures according to a probability level associated with a threshold pseudo-trace length. A simple function that accepts or rejects traces based on a probability level is the log-logistic distribution function:

$$F(l) = \frac{1}{1 + (l/\alpha)^{-\beta}}, l > 0 \tag{36}$$

where α is a scale parameter with units of length that is the trace length with a 50% chance of being observed according to the experimental protocol (e.g., ground sampling distance, operator’s skills, etc.); β is a dimensionless parameter that controls the filter steepness. Low values of β indicate both a large operation range and a low slope, while high β values indicate a sharp transition.

The filter in Eq. (36) is calibrated through probabilistic optimization. The starting point is the histogram of simulated pseudo-trace lengths for a certain trace map. Each trace has its respective length and, therefore, a probability level of being or not being observed by the operator according to Eq. (36). α and β are estimated such that experimental and simulated pseudo-trace length histograms match. A randomized algorithm based on the `binornd.m` routine has been developed in MATLAB. It consists in sampling

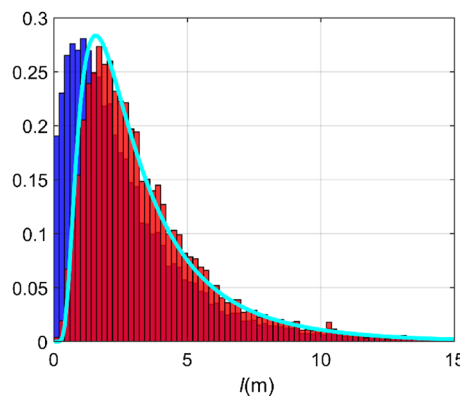


Fig. 10 Probabilistic filter with $\alpha = 1.039$ m and $\beta = 2.375$ for pseudo-trace lengths of TM3. Histogram of simulated pseudo-traces (blue), histogram of likely observed pseudo-traces (red) and marginal KDE (cyan line) of the observed traces

a Bernoulli distribution with a vector composed of n probabilities, n being the number of disks that intersect the surface. The result is a logical vector with 0 when the trace is not observed and 1 when the trace is observed. This process is repeated one thousand times for the whole set of pseudo-trace lengths in each highwall face; for each of those realizations, a Kolmogorov–Smirnov test between the experimental and simulated histograms is performed. The average of the test P values is the parameter to be maximized. The number of disks deemed observed after this filtering is N . Figure 10 shows as an example the effect of the probabilistic filter in the simulated pseudo-trace lengths of TM3. Note that there are many small traces that have not been observed as their sizes were probably below the resolution of the experimental discontinuity detection system.

4 Model Calibration and Results

The objective of the model is to estimate the value of fracture intensity P_{30} that replicates the experimental P_{21} value for each trace map. The process followed to calibrate the DFN model is summarized in Appendix C; (i) Bandwidths h and g are calculated according to Eqs. (10), (11) and (12). (ii) The pseudo-trace length KDE for each orientation is calculated using Eq. (6). (iii) The distribution of disk sizes is estimated through Eqs. (18), (21) and (22); an initial value 0.3 is chosen for the ratio p between semi-bounded traces and the total number of traces. (iv) A large number of disks are sampled according to Eqs. (26) and (30) within a domain large enough to engulf each outcrop; a cubic volume of 40 m side and two million disks (equivalent to a P_{30} of 31.25 m^{-3}) are considered initially. The exponent γ of the weighting function in Eq. (35) is initially set to 1 for all the faces. In a

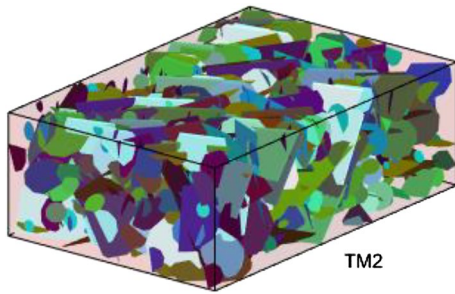


Fig. 11 DFN model for trace map TM2. Disks in inverse pole figure color code (fractures with similar orientation in similar tone)

second iteration, p and γ are recalculated from the results of the previous iteration: p is obtained by counting the number of semi-bounded traces over the total number of traces and γ by following the procedure described in Sect. 3.3.3. These values are checked for convergence:

$$|p_i - p_{i-1}| \wedge |\gamma_i - \gamma_{i-1}| < \epsilon \tag{37}$$

Steps (iii) to (iv) are repeated until convergence. Then (v) the probabilistic truncation process in Sect. 3.4 is applied to fit the truncation function parameters α and β in Eq. (36). The resulting mean number of traces that intersect the face after applying the probabilistic filter, N , is obtained in this process.

An estimator of P_{30} , i.e., number of disks to be simulated within the domain to obtain the P_{21} observed on the surface in the field is:

$$\hat{P}_{30} = \lceil \frac{\sum_i l_i}{\bar{l}} / \frac{N}{TF} \rceil / V \tag{38}$$

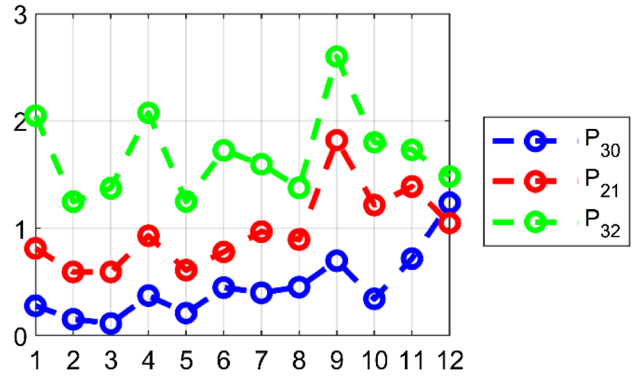


Fig. 12 Fracture intensity parameters P_{30} , P_{21} and P_{32} for the faces studied

where l_i is the pseudo-trace length of a trace observed experimentally, \bar{l} is the mean of the pseudo-trace length KDE, TF is the total number of fractures generated within the domain and V the volume of the domain.

The parameters of the model (h , g , p , γ , α and β) are summarized in Table 4 for the twelve highwall faces. Fracture intensities P_{30} , P_{21} and P_{32} are given and also the percentage of fractures that intersect the outcrop over the total number of disks generated, N/TF . An example of DFN model is shown in Fig. 11, see others in Fig. 20, Appendix B. The scale parameter α of the log-logistic function, Eq. (36), decreases from TM1 to TM12 (Table 4). This implies that shorter traces are marked for the last faces. This might be likely caused either by local changes in rock mass due to the existence of the extensional fault that crosses the high-wall faces TM11 and TM12, see Bernardini et al. (2022) for additional information. Figure 12 shows the fracturing intensity parameters for the twelve trace maps. They are in

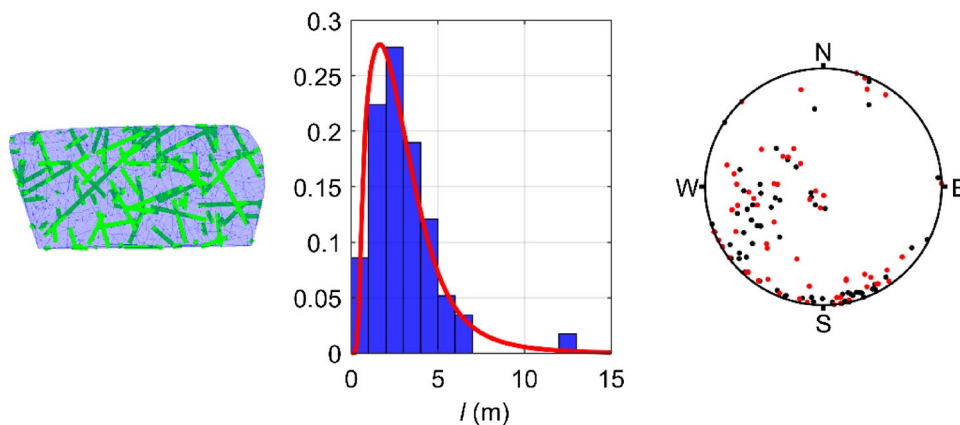
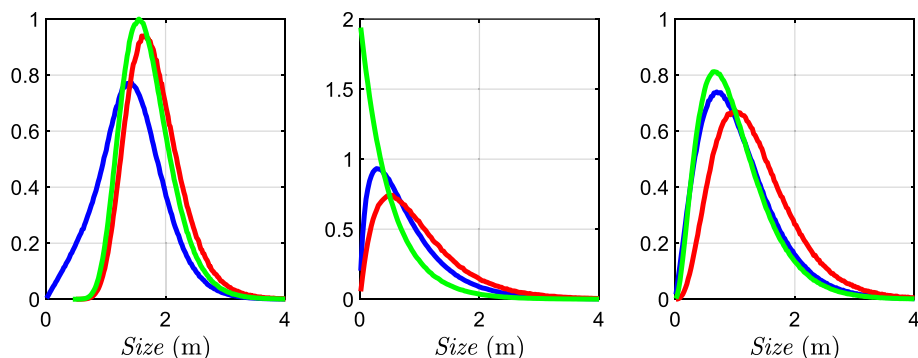


Fig. 13 Model results for face TM1. Left: pseudo-traces, shown as green segments (the surface has some transparency and darker lines are pseudo-traces located behind the surface). Center: marginal KDE of pseudo-trace lengths obtained from experimental data (red curve:

experimental; blue bars: histogram of pseudo-trace lengths from the simulation). Right: map of experimental (black dots) and simulated (red dots) poles (colour figure online)

Fig. 14 Lognormal (left), negative exponential (center) and gamma (right) distributions of true disk sizes (green), size of disks that intersect the surface (red) and pseudo-trace lengths (blue) (colour figure online)



general higher for faces in DS2 domain (TM7–TM12), and they all follow a similar trend except in TM11 and TM12, where P_{30} increases and P_{21} and P_{32} do not. This may be explained as Table 1 shows due to an increase in the number of fractures, and a decrease in their mean sizes (raised to the second power), especially in TM12.

To illustrate the model performance, Fig. 13 shows, for TM1: traces (chords) obtained from a simulation (green lines in the left graph); the marginal KDE of pseudo-trace lengths obtained from experimental data (red curve in the central graph), together with the histogram of pseudo-trace lengths obtained from the simulation (blue bars); and the map of experimental and simulated poles (black and red dots, respectively, right graph). The model is stochastically similar to the observations. The number of fractures observed to intersect the surface is 66 that coincides with the average number of simulated disks that intersect the surface. All other cases are shown in Fig. 16.

5 Discussion

To assess the validity of the proposed DFN model, the relations proposed by Zhang et al. (2002) for trace lengths and disk sizes must be verified and typical relations among fracture intensities must be met.

The common relations between true disk sizes and pseudo-trace lengths distributions Zhang et al. (2002) have been used to assess Eq. (17) in Sect. 3.2. Such relations were derived for some common distributions of trace length, such as lognormal, negative exponential and gamma, assuming

Table 2 Relation between parameters (mean, m and variance, v) of the true disk size (subscript D) and the pseudo-trace length (subscript L) distributions; same colors as in Fig. 14 have been used

True disk size distribution	m_D	m_L	v_D	v_L
Lognormal	1.701	1.422	0.187	0.304
Negative exponential	0.500	0.786	0.250	0.383
Gamma	1.000	1.048	0.334	0.387

the same distribution for both disk size and pseudo-trace length. Three numerical simulations have been performed with disk sizes following: (i) a lognormal distribution with $\mu=0.5$ m and $\sigma=0.25$ m, (ii) a negative exponential distribution with $\mu=0.25$ m, and (iii) a gamma distribution with $\alpha=2$ and $\beta=0.5$. The resultant distributions obtained with Eqs. (17) and (35) are shown in Fig. 14. Green histograms correspond to the true disk size distribution and the blue ones the pseudo-trace lengths. The distributions of disks that intersect the surface have also been plotted (red), as these distributions are used for calculating the pseudo-trace lengths. Table 2 summarizes the means and variances (m and v) of the different distributions obtained in the simulations. They are asymptotically equal to those obtained from the relationships provided by Zhang et al. (2002) (for a two million disk simulation they are equal to the third significant digit). Note in Fig. 14 that the distribution type of disk sizes

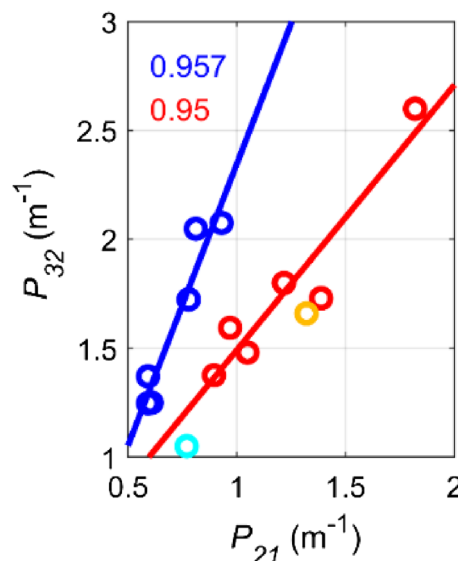


Fig. 15 Linear correlations between P_{32} and P_{21} for the 12 highwall faces studied. DS1 (blue and cyan) and DS2 (red and orange) (colour figure online)

and traces is not necessarily preserved; this is quite obvious for the lognormal and the negative exponential cases. Even if the means and variances are well estimated, the actual distributions can be grossly different.

A linear relationship would be expected between the fracture intensities P_{21} and P_{32} for domains with similar properties (Dershowitz and Herda 1992; Mauldon 1994; Wang 2005), with a ratio P_{21}/P_{32} between 0 and 1. This applies irrespective of the disk size distribution. To verify this, values of P_{32} and P_{21} from Table 4 have been plotted, grouping them by the domain they belong to, in Fig. 15. Values of P_{21}/P_{32} are also given in Table 4. Correlation coefficients are shown in the upper left part of the graph. Both P values are lower than 0.05 which indicates the relations are significant. The same relations were tried between P_{30} and P_{21} , and P_{30} and P_{32} , in this case without significance to the 0.05 level. P_{30} provides an incomplete fracture description as it only indicates the density of support points while the size of the fractures (unlike P_{21} and P_{32}) is missing in it. In fact, there is probably no reason for P_{30} to be correlated, in general, with P_{32} or P_{21} though, for a given size distribution of fractures, more fractures will likely encompass more traces (and longer total trace length) on an intersecting surface, and more fracture surface per unit volume. To assess differences between the model developed in this work and traditional DFN models, fracture densities of the domains DS1 and DS2 built with FracMan[®] suite Bernardini et al. (2022) are plotted for comparison, as cyan and orange points, in Fig. 15. They fall acceptably well in the linear trends of each pair of fracture densities, especially for the DS2 case (red and orange points).

The use of traditional DFN codes implies inevitably: (i) initial manual sectorization of fractures, which may introduce some bias because of the operator's criterion; to this, the time spent in interpreting the data must be added; (ii) parametrical characterization of the families, which involves selecting some probability distribution functions based on Kolmogorov–Smirnov tests; and (iii) calibration of an intensity parameter for each family of fractures, which entails increasing computational time with increasing number of families. In our own experience with traditional codes, the third step consumes the most computational time. The calibration process of the model proposed here saves considerable amounts of time in this step, since the KDEs considers all fractures independently of the family they might belong to. As an example, the computational time the code consumes in completing an iteration for TM10 is about 75 min on a 2.2 GHz MSI GF62 8RD laptop. Most of the time, 65.2%, is spent in solving the triangle–triangle intersections that is dependent of the quantity of disks, the number of sides of each disk and the number of triangles that make up the intersection surface, a 21% in self-time (third step in

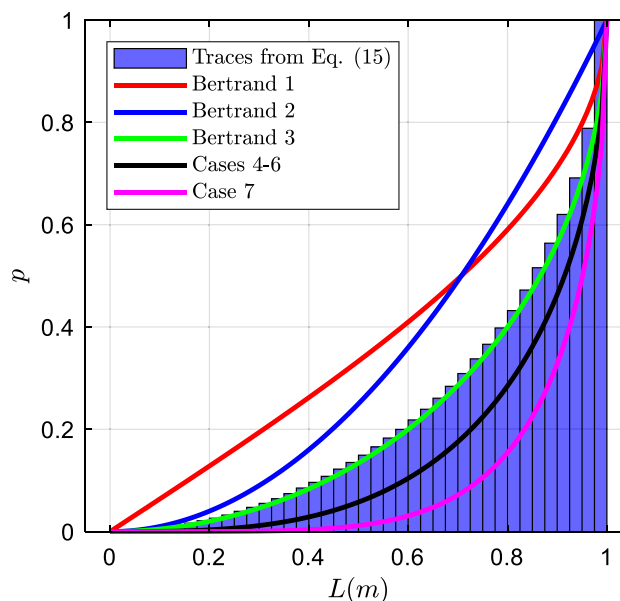


Fig. 16 Pseudo-trace length distribution resultant from 1 m diameter disks. Results from randomly evaluating Eq. (15) (blue histogram) and from the distribution functions in Table 3

Sect. 4), a 5.5% in calibrating the probabilistic filter, a 5.3% in random sampling and the rest in other subroutines.

6 Conclusions

A novel distribution-free DFN generation technique is developed, making use of directional-linear KDE to non-parametrically characterize jointly the distribution of fracture orientations and trace lengths. The non-parametric approach does not require a classification of fractures into sets as parametric models do and does not demand any statement on a particular functional distribution of trace lengths or disk diameters derived thereof.

The mathematical modeling and the application steps are explained thoroughly, with the inclusion of numerical tests of consistency where required. Bias corrections are provided for censoring, size, orientation and truncation. Censoring is addressed using a new calculation method that includes semi-bounded traces. Size and orientation biases are jointly addressed using a new weighting function. The truncation bias is corrected by a probabilistic filter capable of incorporating fractures to the DFN shorter than those observed in field measurements. This endows the model with a certain scale-independent character, not the case of traditional parametric DFN models.

The model has been applied to twelve trace maps obtained from photogrammetry of highwall faces. Disk orientations

were obtained by fitting a plane to the 3D-polyline defined by the traces. The DFN models are calibrated using Monte Carlo realizations of the non-parametric distributions. A Poisson point process is used for fractures location, assumed to be flat and circular in shape. Solution No. 3 of the Bertrand paradox has proved to be effective to estimate disk sizes from trace lengths.

The experimental value of P_{2l} , is fitted through the number of fractures per unit volume (P_{30}). The resulting fracture intensities P_{2l} and P_{32} are linearly related, which supports the model validity. These intensities have been discussed with classical DFN generation systems.

While the non-parametric model does not require an assumption of a distribution type for traces and fracture diameters, its results meet the classical relations between mean and variance of trace lengths and disk diameters. It is shown however, that the distribution types of trace lengths and diameters can be markedly different, a feature that does not affect kernel-based non-parametric DFNs.

Appendix A. Proofs

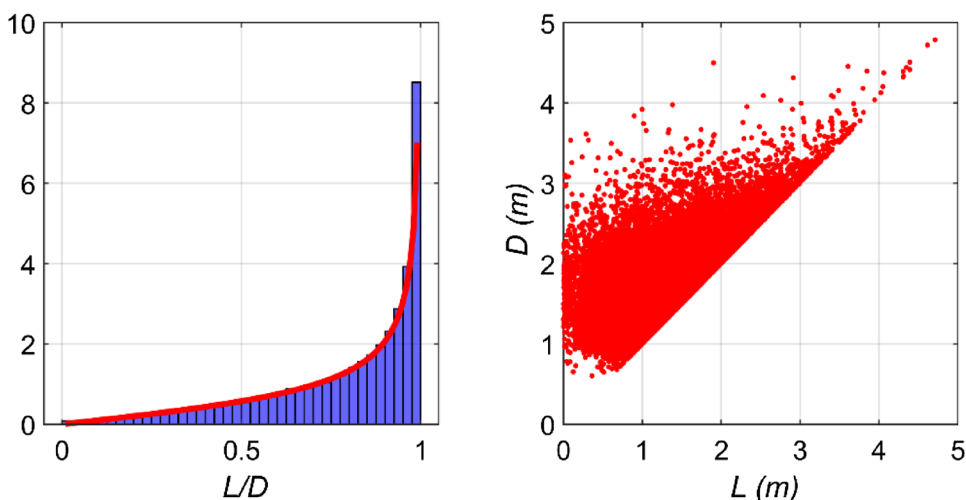
In this appendix different proofs mentioned in the manuscript are exposed.

A.1 Warburton’s Relationship Derivation

Consider two independent random variables X and Y . The resultant product distribution of a new random variable Z is:

$$f_Z(z) = \int_{-\infty}^{\infty} f_X(x)f_Y(z/x) \frac{1}{|x|} dx \tag{39}$$

Fig. 17 Left: density function of the variable $Y = L/D$, Eq. (16); numerical values (blue histogram) and density function of Eq. (17) (red line). Right: Relation of pseudo-trace length vs. diameter (colour figure online)



Taking the density function in Eq. (22) as the distribution of the random variable Y , the density function of X as the weighed disk size density function and Z as the pseudo-trace length density function, one may write:

$$f_L(L) = \int_{-\infty}^{\infty} \frac{f_D(D) \cdot w(D) \cdot L}{E[w(D)] \cdot D \cdot |D| \cdot \sqrt{1 - (L/D)^2}} dD \tag{40}$$

Since for infinite outcrops the weighing function $w(D) = D$ and $E[w(D)]$ is a constant, then the previous equation may be simplified to:

$$f_L(L) = \frac{L}{E[w(D)]} \int_{-\infty}^{\infty} \frac{f_D(D)}{|D| \sqrt{1 - (L/D)^2}} dD \tag{41}$$

Regarding integration limits, none of the functions are defined for negative values. Furthermore, as any pseudo-trace length is obtained from disks with size larger than the pseudo-trace itself, then Eq. (B.3) may be written:

$$f_L(L) = \frac{L}{E[w(D)]} \int_L^{\infty} \frac{f_D(D)}{\sqrt{D^2 - L^2}} dD \tag{42}$$

Note the similarity of this equation with the relation obtained by Warburton (1980a).

A.2 Relationship Between Eq. (15) and Bertrand Paradox Number 3

The distribution of Eq. (15) is consistent with the distribution function obtained from Aldous et al. (1988) and Chiu and Larson (2009) for Bertrand’s paradox number 3. Taking for instance disks of diameter $D = 1$ m, Fig. 16 compares the results from randomly sampling Eq. (15) and Bertrand’s distribution functions together with some sources

Table 3 Statistics of random chord lengths of cases 1–7 described by Chiu and Larson (2009). Main statistics are obtained making $r=1$

	Bertrand 1: two points on circumference Case 1	Bertrand 2: chord center inside circle Case 2	Bertrand 3: chord center on radius Case 3	One point on circumfer- ence, one inside Cases 4–6	Both points inside circle Case 7
Density function $L \in [0, 2r]$	$\frac{2}{\pi\sqrt{4r^2-L^2}}$	$\frac{L}{2r^2}$	$\frac{L}{2r\sqrt{4r^2-L^2}}$	$\frac{L^2}{\pi r^2\sqrt{4r^2-L^2}}$	$\frac{1}{3\pi\sqrt{4r^2-L^2}}\left(\frac{L}{r}\right)^4$
Distribution function $L \in [0, 2r]$	$\frac{2}{\pi}\sin^{-1}\left(\frac{L}{2r}\right)$	$\frac{L^2}{4r^2}$	$1 - \frac{\sqrt{4r^2-L^2}}{2r}$	$\frac{2}{\pi}\left[\sin^{-1}\left(\frac{L}{2r}\right) - \frac{L\sqrt{4r^2-L^2}}{4r^2}\right]$	$\frac{2}{\pi}\cos^{-1}\left(\frac{\sqrt{4r^2-L^2}}{2r}\right) - \frac{L(6r^2+L^2)\sqrt{4r^2-L^2}}{12\pi r^4}$
Bertrand probability $P(L > \sqrt{3})$	1/3	1/4	1/2	0.609	0.7468
Median	$\sqrt{2}$	$\sqrt{2}$	$\sqrt{3}$	1.8295	1.9021
Mean	$4/\pi$	$4/3$	$\pi/2$	$16/3\pi$	$256/45\pi$
Standard deviation	$\sqrt{2-16/\pi^2}$	$\sqrt{2/3}$	$(1/4)\sqrt{\pi(\pi^2-8)}$	$\sqrt{(3-256/9\pi^2)}$	$\sqrt{(10/3-65536/2025\pi^2)}$

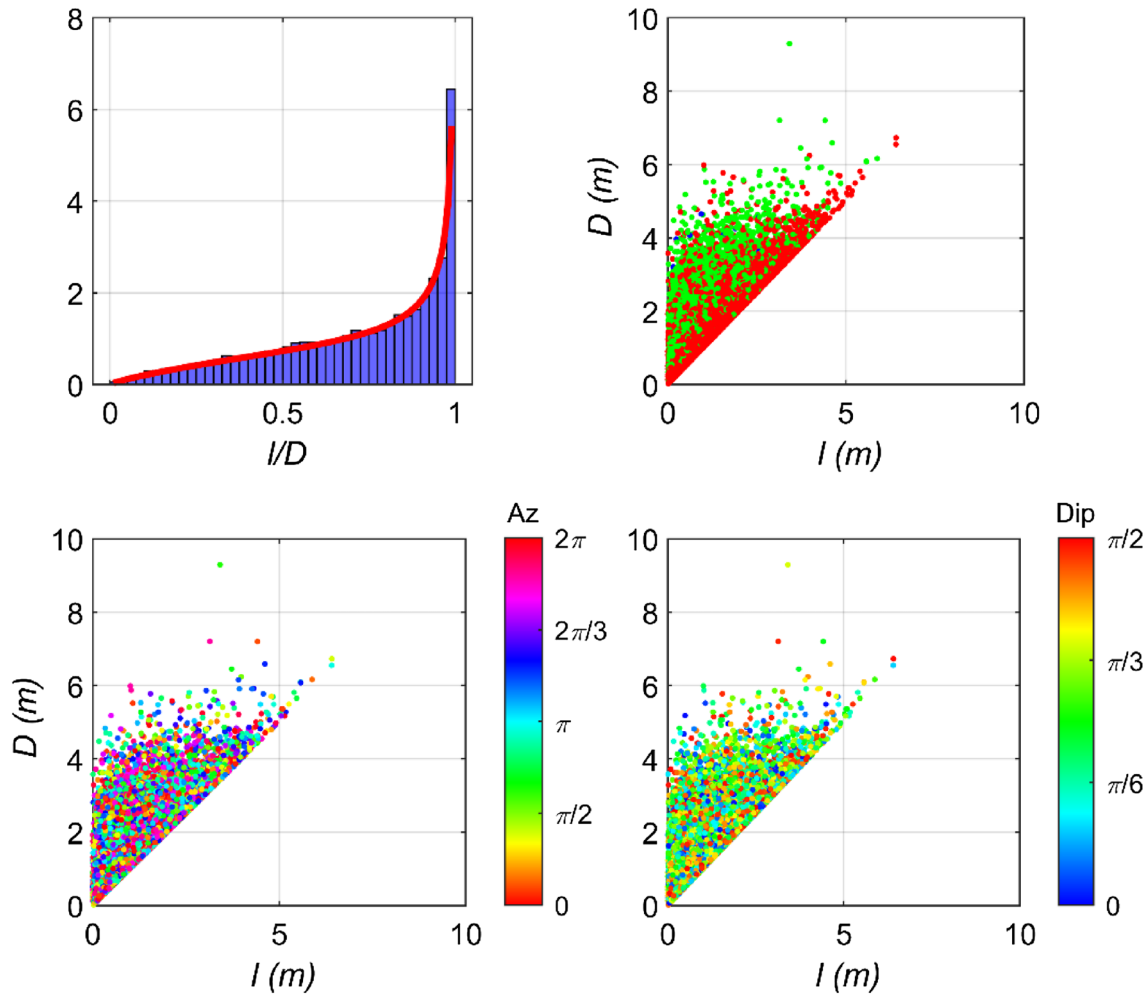


Fig. 18 Upper left: density function of Ψ ; numerical values (blue histogram) and Eq. (20) (red line). The other graphs: relation between incomplete pseudo-trace lengths and their respective diameters, with color points coded differently: upper right, according to their trace type (red, green and blue dots are complete, semi-bounded and

bounded traces respectively); lower left, according to their dip direction; lower right: according to their dip angle. In the lower graphs, colors correspond to the scales on the right of the plots (colour figure online)

of randomness (cases 4 to 7) discussed by Chiu and Larson (2009) (see Table 3). One may note that Eq. (15) and Bertrand 3 (green line) are clearly equivalent. The same works for any other diameter.

A.3 Numerical Simulation to Prove the Validity of Eq. (17)

Five hundred thousand disks with random orientations were distributed inside a cubic domain with 10 m side, following a Poisson process. Their sizes were assumed to be distributed following a lognormal distribution with parameters $\mu=0.5$ m and $\sigma=0.25$ m so that they never exceeded the extension of a finite rectangular surface of 30×30 m. The resulting traces were divided by their respective disk sizes. Figure 17 shows the histogram of L/D (blue bars) obtained with Eq. (18) and the analytical probability distribution in Eq. (17) (red line). Red points in the right graph show the complete trace lengths corresponding to their disk sizes. The result is quite satisfactory.

A.4 Numerical Simulation to Prove the Validity of Eq. (20)

Disks with random orientations and following a Poisson process were generated within a 10 m side cubic domain so that they intersect a 5 m-radius circumferential outcrop. disk sizes

may be set to follow any distribution used in the literature for trace lengths; take for example a gamma distribution with parameters $\alpha=2$ and $\beta=0.5$. To the extent possible, these parameters were chosen in a way that the size of the surface is large compared to disk sizes, leading to a limited number of bounded traces. The result of the test is shown in Fig. 18. The graph on the upper left shows the histogram of l/D (blue bars) and the density function f_{ψ} (red line) with p taking a value of 0.2. P has been obtained from the upper right graph, calculating the proportion of semi-bounded traces over the total number of traces. In this graph, l values are represented vs. disk size D ; red, green and blue dots in the upper plot indicate complete, semi-bounded and bounded traces, respectively. The result is, again, satisfactory.

Orientation and dip have also been plotted to check independence between the random variables, see bottom graphs in Fig. 18. Orientations are randomly distributed, without a preferential pattern.

Appendix B. Results

Table 4 and Figs. 19, 20 summarize the main results of the model developed in this paper.

Table 4 DFN results

Trace map	Bandwidths		P	γ	Log-logistic truncation			DFN results					
	h	g			α (m)	β	P value	N/TF (%)	P_{30} (m^{-3})	Area (m^2)	$P_{21,sim}$ (m^{-1})	$P_{32,sim}$ (m^{-1})	P_{21}/P_{32}
TM1	0.13	0.35	0.37	1.33	1.17	2.27	0.72	0.37	0.276	230.2	0.81	2.05	0.40
TM2	0.16	0.23	0.36	1.42	1.53	3.03	0.71	0.49	0.151	268.1	0.59	1.25	0.47
TM3	0.19	0.40	0.43	1.13	1.04	2.38	0.84	0.70	0.111	264.7	0.59	1.37	0.43
TM4	0.16	0.37	0.31	1.21	0.75	2.74	0.99	0.38	0.372	234.5	0.93	2.08	0.45
TM5	0.15	0.66	0.30	1.28	0.87	2.69	0.91	0.44	0.208	247.2	0.61	1.25	0.49
TM6	0.17	0.30	0.27	1.48	0.98	2.31	0.83	0.26	0.447	199.7	0.78	1.72	0.45
TM7	0.12	0.40	0.28	1.34	0.62	2.91	0.99	0.55	0.398	307.3	0.97	1.59	0.61
TM8	0.13	0.50	0.23	1.17	0.30	2.81	0.97	0.57	0.451	338.9	0.90	1.38	0.65
TM9	0.14	0.59	0.28	1.30	0.34	2.57	0.95	0.54	0.697	314.2	1.82	2.60	0.70
TM10	0.13	0.69	0.29	1.22	0.23	3.00	0.99	0.77	0.341	389.0	1.22	1.80	0.68
TM11	0.12	0.61	0.30	1.24	0.23	4.73	0.96	0.36	0.717	308.6	1.39	1.73	0.80
TM12	0.14	0.51	0.18	1.22	0.17	2.56	0.99	0.26	1.237	274.8	1.05	1.48	0.71

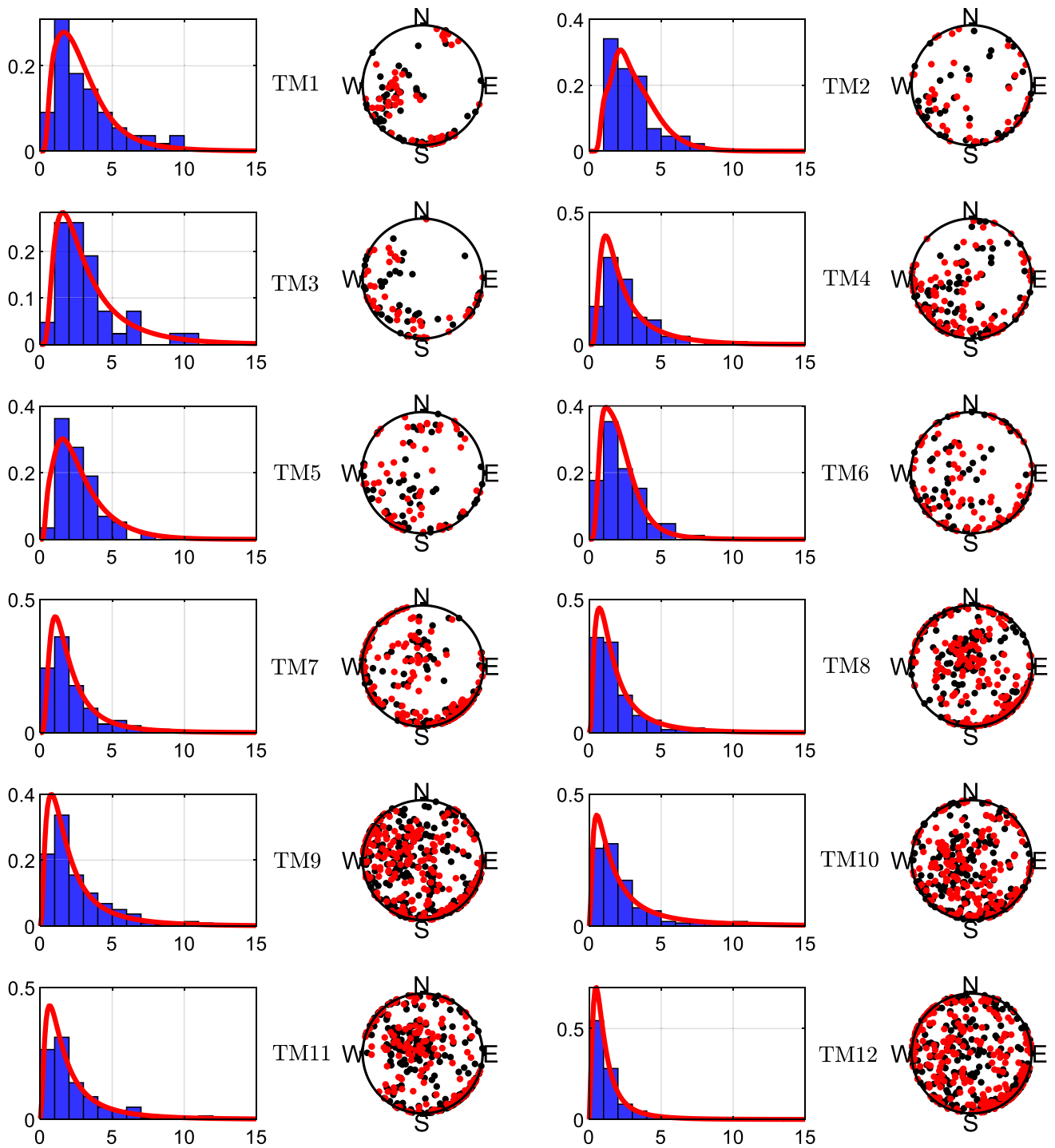


Fig. 19 Simulated pseudo-trace lengths (blue bar histograms), experimental KDE of pseudo-trace lengths (red lines), experimental poles (black dots) and simulated poles (red dots) (colour figure online)

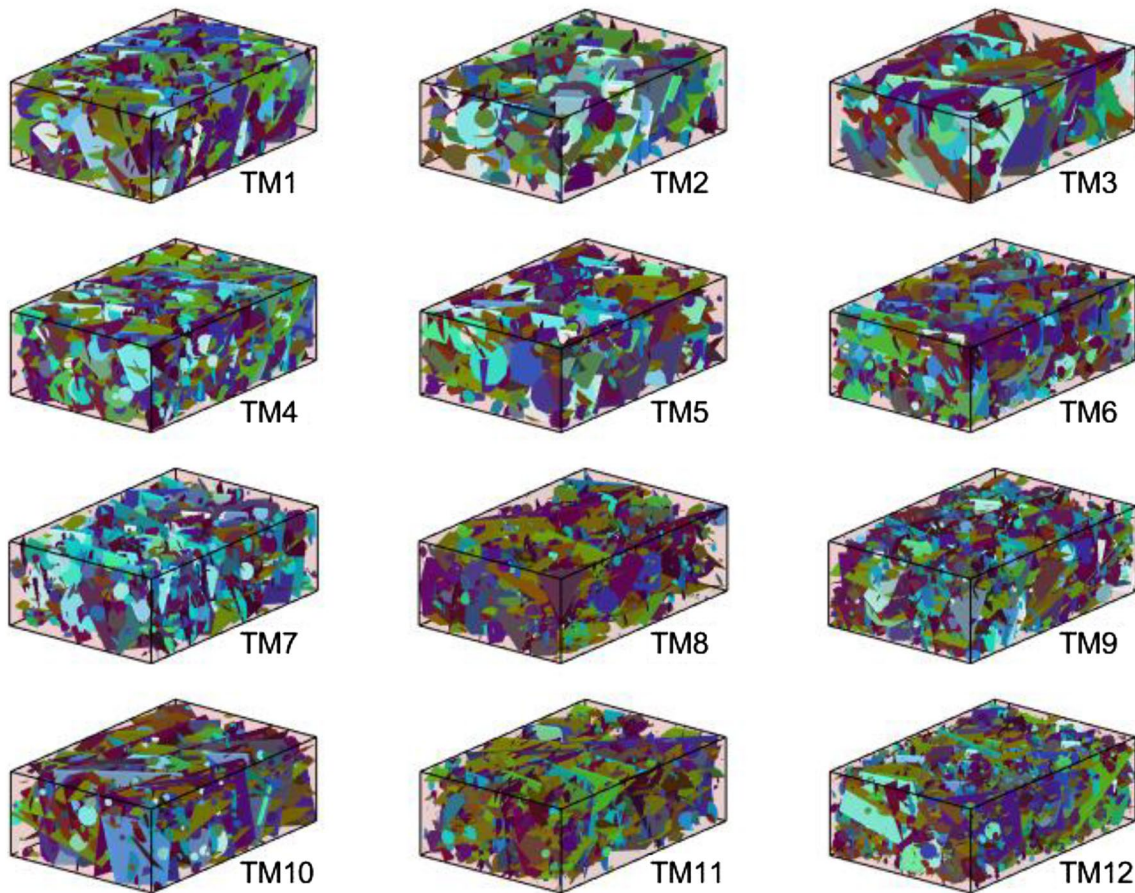


Fig. 20 Simulated DFN models in domains with size $30 \times 20 \times 10$ m. Fractures with similar orientations are colored with similar tones using an inverse pole figure color code

Appendix C. Flowchart of the calculation process

The process followed to calibrate the DFN model is summarized in Fig. 21.

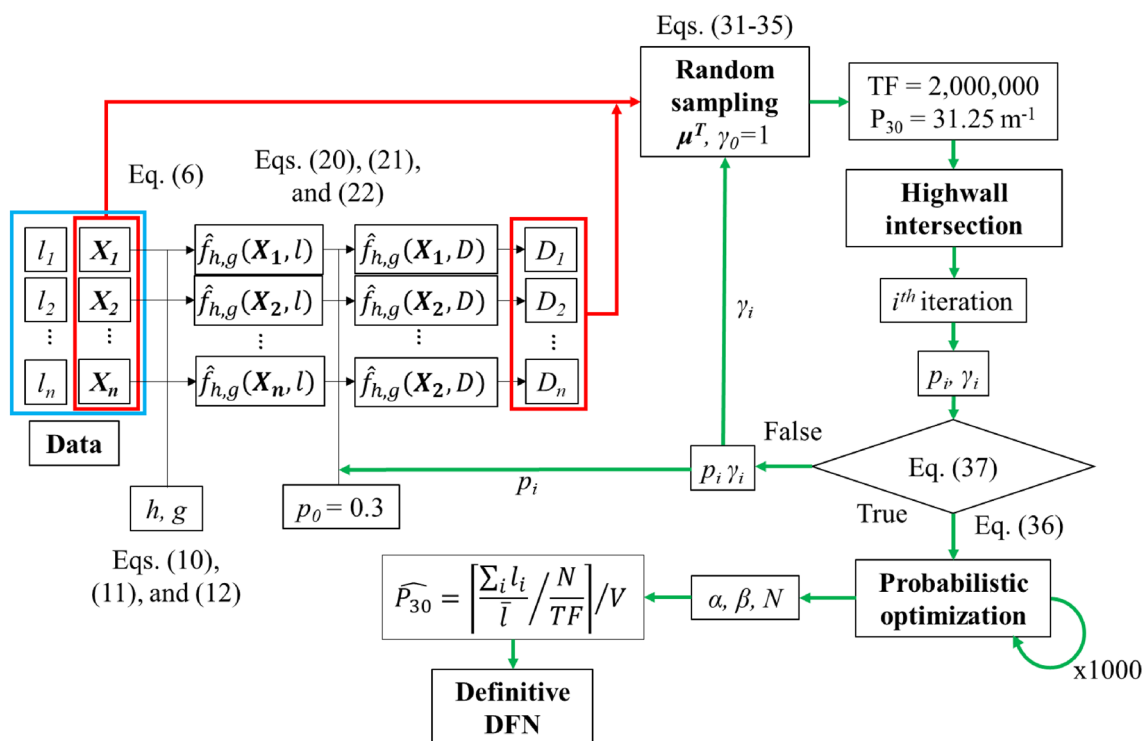


Fig. 21 Flowchart to build the non-parametric Poisson-disc DFN model

Acknowledgements This work has been conducted under the SLIM and DIGIECOQUARRY projects funded by the European Union's Horizon 2020 research and innovation program under grant agreements no. 730294 and 101003750.

Funding Open Access funding provided thanks to the CRUE-CSIC agreement with Springer Nature.

Data availability The data that support the findings of this study are available in a Zenodo repository <https://doi.org/10.5281/zenodo.7533565>.

Declarations

Conflict of Interest The authors declare that they have no conflict of interest.

Ethical Approval Not applicable.

Consent to Participate Not applicable.

Consent for Publication Not applicable.

Open Access This article is licensed under a Creative Commons Attribution 4.0 International License, which permits use, sharing, adaptation, distribution and reproduction in any medium or format, as long as you give appropriate credit to the original author(s) and the source, provide a link to the Creative Commons licence, and indicate if changes were made. The images or other third party material in this article are included in the article's Creative Commons licence, unless indicated otherwise in a credit line to the material. If material is not included in the article's Creative Commons licence and your intended use is not

permitted by statutory regulation or exceeds the permitted use, you will need to obtain permission directly from the copyright holder. To view a copy of this licence, visit <http://creativecommons.org/licenses/by/4.0/>.

References

- Aldous D, Stoyan D, Kendall WS, Mecke J (1988) Stochastic geometry and its applications. J Am Stat Assoc. <https://doi.org/10.2307/2288885>
- Andersson J, Shapiro AM, Bear J (1984) A stochastic model of a fractured rock conditioned by measured information. Water Resour 20(1):79–88. <https://doi.org/10.1029/WR020i001p00079>
- Baecher GB (1983) Statistical analysis of rock mass fracturing. J Int Assoc Math Geol 15(2):329–348. <https://doi.org/10.1007/BF01036074>
- Baecher G, Lanney N (1978) Trace length biases in joint surveys. 19th US symposium on rock mechanics (USRMS), Reno, Nevada
- Baecher G, Lanney N, Einstein H (1977) Statistical description of rock properties and sampling. The 18th US Symposium on Rock Mechanics (USRMS). Golden, Colorado
- Bernardini M, Paredes C, Sanchidrián JA, Segarra P, Gómez S (2022) The influence of the sampling scale on the in-situ block size distribution. Rock Mech Rock Eng. <https://doi.org/10.1007/s00603-022-02953-1>
- Bertrand J (1888) Calcul des probabilités, 1889th edn. Gauthier-Vilars et fils, Paris
- Bingham C (1964) Distributions on the sphere and on the projective plane. Doctoral dissertation
- Bonilla-Sierra V, Scholtès L, Donzé FV, Elmoutie MK (2015) Rock slope stability analysis using photogrammetric data and

- DFN–DEM modelling. *Acta Geotech* 10(4):497–511. <https://doi.org/10.1007/s11440-015-0374-z>
- Chilès J-P, de Marsily G (1993) Stochastic models of fracture systems and their use in flow and transport modeling. Flow and contaminant transport in fractured rock. <https://doi.org/10.1016/b978-0-12-083980-3.50008-5>
- Chiu S, Larson R (2009) Bertrand's Paradox Revisited: More Lessons about that Ambiguous Word, Random. *J Ind Syst* 3(1):1–26. https://www.researchgate.net/profile/Richard_Larson5/publication/266293651_Bertrand's_Paradox_Revisited_More_Lessons_about_that_Ambiguous_Word_Random/links/54d9e7d20cf24647581fbf3a.pdf. Retrieved 6 May 6 2021
- Dershowitz WS, Herda HH (1992) Interpretation of fracture spacing and intensity. In the 33rd U.S. symposium on rock mechanics (USRMS). Santa Fe, New Mexico
- Dershowitz WS, Einstein HH (1988) Characterizing rock joint geometry with joint system models. *Rock Mech Rock Eng* 21(1):21–51. <https://doi.org/10.1007/BF01019674>
- Elmo D, Stead D, Rogers S (2015) Guidelines for the quantitative description of discontinuities for use in discrete fracture network modelling. 13th ISRM international congress of rock mechanics. International Society for Rock Mechanics and Rock Engineering, Montreal
- Elmoultie MK, Poropat GV (2012) A method to estimate in situ block size distribution. *Rock Mech Rock Eng* 45(3):401–407. <https://doi.org/10.1007/s00603-011-0175-0>
- Fisher N, Lewis T, Embleton B (1993) Statistical analysis of spherical data. Cambridge University Press
- García-Portugués E (2013) Exact risk improvement of bandwidth selectors for kernel density estimation with directional data. *Electron J Stat* 7(1):1655–1685. <https://doi.org/10.1214/13-EJS821>
- García-Portugués E, Crujeiras RM, González-Manteiga W (2013) Kernel density estimation for directional-linear data. *J Multivar Anal* 121:152–175. <https://doi.org/10.1016/j.jmva.2013.06.009>
- Geenens G, Wang C (2018) Local-likelihood transformation Kernel density estimation for positive random variables. *J Comput Graph Stat* 27(4):822–835. <https://doi.org/10.1080/10618600.2018.1424636>
- Golder Associates Inc (2018) FracMan7-interactive discrete feature data analysis, geomtric modeling and exploration simulation user documentation version 7.7. Golder Associates Inc, Redmond
- Guo J, Zheng J, Lü Q, Deng J (2022) Estimation of fracture size and azimuth in the universal elliptical disc model based on trace information. *J Rock Mech Geotech Eng*. <https://doi.org/10.1016/j.jrmge.2022.07.018>
- Hekmatnejad A, Emery X, Vallejos JA (2018) Robust estimation of the fracture diameter distribution from the true trace length distribution in the Poisson-disc discrete fracture network model. *Comput Geotech* 95(April 2017):137–146. <https://doi.org/10.1016/j.compgeo.2017.09.018>
- Hekmatnejad A, Emery X, Elmo D (2019) A geostatistical approach to estimating the parameters of a 3D Cox-Boolean discrete fracture network from 1D and 2D sampling observations. *Int J Rock Mech Min Sci* 113(November 2018):183–190. <https://doi.org/10.1016/j.ijrmms.2018.11.003>
- Hunziker J, Favino M, Caspari E, Quintal B, Rubino JG, Krause R, Holliger K (2018) Seismic attenuation and stiffness modulus dispersion in porous rocks containing stochastic fracture networks. *J Geophys Res* 123(1):125–143. <https://doi.org/10.1002/2017JB014566>
- ISRM (1978) Suggested methods for the quantitative description of discontinuities in rock masses. *Int J Rock Mech Min Sci Geomech Abstr* 16(2):22. [https://doi.org/10.1016/0148-9062\(79\)91476-1](https://doi.org/10.1016/0148-9062(79)91476-1)
- Jimenez-Rodriguez R, Sitar N (2006) Inference of discontinuity trace length distributions using statistical graphical models. *Int J Rock Mech Min Sci* 43(6):877–893. <https://doi.org/10.1016/j.ijrmms.2005.12.008>
- Keilegavlen E, Berge R, Fumagalli A, Starnoni M, Stefansson I, Varela J, Berre I (2021) PorePy: an open-source software for simulation of multiphysics processes in fractured porous media. *Comput Geosci* 25(1):243–265. <https://doi.org/10.1007/s10596-020-10002-5>
- Kulatilake P, Wu T (1984) Estimation of mean trace length of discontinuities. *Rock Mech Rock Eng* 17(4):215–232. <https://doi.org/10.1007/BF01032335>
- Kulatilake PHSW, Um JG, Wang M, Escandon RF, Narvaiz J (2003) Stochastic fracture geometry modeling in 3-D including validations for a part of Arrowhead East Tunnel, California, USA. *Eng Geol* 70(1–2):131–155. [https://doi.org/10.1016/S0013-7952\(03\)00087-5](https://doi.org/10.1016/S0013-7952(03)00087-5)
- Laslett G (1982) Censoring and edge effects in areal and line transect sampling of rock joint traces. *J Int Assoc Math Geol* 14(2):125–140
- Lee CC, Lee CH, Yeh HF, Lin HI (2011) Modeling spatial fracture intensity as a control on flow in fractured rock. *Environ Earth Sci* 63(6):1199–1211. <https://doi.org/10.1007/s12665-010-0794-x>
- Lei Q, Latham JP, Tsang CF (2017) The use of discrete fracture networks for modelling coupled geomechanical and hydrological behaviour of fractured rocks. *Comput Geotech* 85:151–176. <https://doi.org/10.1016/j.compgeo.2016.12.024>
- Long JCS, Remer JS, Wilson CR, Witherspoon PA (1982) Porous media equivalents for networks of discontinuous fractures. *Water Resour Res* 18(3):645–658. <https://doi.org/10.1029/WR018i003p00645>
- Lu P (1997) The characterisation and analysis of in-situ and blasted rock size distributions and blastability. Doctoral disertation
- MATLAB (2019) MATLAB R2019b, version 9.7.0. The MathWorks Inc, Natick, Massachusetts
- Mauldon M (1994) Intersection probabilities of impersistent joints. *Int J Rock Mech Min Sci* 31(2):107–115. [https://doi.org/10.1016/0148-9062\(94\)92800-2](https://doi.org/10.1016/0148-9062(94)92800-2)
- Mauldon W, Xiaohai M (2006). Proportional errors of the Terzaghi correction factor. Proceedings of the 41st US. Rock Mechanics Symposium–ARMA's Golden Rocks 2006-50 Years of Rock Mechanics (January 2006)
- Miyoshi T, Elmo D, Rogers S (2018) Influence of data analysis when exploiting DFN model representation in the application of rock mass classification systems. *J Rock Mech Geotech Eng* 10(6):1046–1062. <https://doi.org/10.1016/j.jrmge.2018.08.003>
- Moller T (1998) Fast triangle-triangle intersection test. *Doktorsavhandlingar Vid Chalmers Tekniska Hogskola* 1425:123–129. <https://doi.org/10.1080/10867651.1997.10487472>
- Ozkaya SI, Mattner J (2003) Fracture connectivity from fracture intersections in borehole image logs. *Comput Geosci* 29(2):143–153. [https://doi.org/10.1016/S0098-3004\(02\)00113-9](https://doi.org/10.1016/S0098-3004(02)00113-9)
- Priest S (1993) Discontinuity analysis for rock engineering, 1st edn. Springer, Netherlands, Dordrecht. <https://doi.org/10.1007/978-94-011-1498-1>
- Priest SD, Hudson JA (1981a) Estimation of discontinuity spacing and trace length using scanline surveys. *Int J Rock Mech Min Sci* 18(3):183–197. [https://doi.org/10.1016/0148-9062\(81\)90973-6](https://doi.org/10.1016/0148-9062(81)90973-6)
- Priest S, Hudson J (1981b) Estimation of discontinuity spacing and trace length using scanline surveys. *Int J Rock Mech Min Sci Geomech Abstr* 18(3):183–197
- Riley MS (2005) Fracture trace length and number distributions from fracture mapping. *J Geophys Res* 110(8):1–16. <https://doi.org/10.1029/2004JB003164>

- Robinson PC (1983) Connectivity of fracture systems—a percolation theory approach. *J Phys A* 16(3):605–614. <https://doi.org/10.1088/0305-4470/16/3/020>
- Saghir A, Hamedani GG, Tazeem S, Khadim A (2017) Weighted distributions: a brief review, perspective and characterizations. *Int J Stat Probab* 6(3):109. <https://doi.org/10.5539/ijsp.v6n3p109>
- Santaló L (1955) Sobre la distribución de los tamaños de corpusculos contenidos en un cuerpo a partir de la distribución en sus secciones o proyecciones. *Trabajos De Estadística* 6(3):181–196
- Semechko, A. (2012). *Suite of functions to perform uniform sampling of a sphere*. Retrieved from <https://www.mathworks.com/matlabcentral/fileexchange/37004-suite-of-functions-to-perform-uniform-sampling-of-a-sphere>
- Song JJ, Lee CI (2001) Estimation of joint length distribution using window sampling. *Int J Rock Mech Min Sci* 38(4):519–528. [https://doi.org/10.1016/S1365-1609\(01\)00018-1](https://doi.org/10.1016/S1365-1609(01)00018-1)
- Tang ZC, Wu ZL, Zou J (2022) Appraisal of the number of asperity peaks, their radii and heights for three-dimensional rock fracture. *Int J Rock Mech Min Sci*. <https://doi.org/10.1016/j.ijrmmms.2022.105080>
- Terzaghi R (1965) Sources of error in joint surveys. *Geotechnique* 15(3):287–304. <https://doi.org/10.1680/geot.1965.15.3.287>
- Tonon F, Chen S (2007) Closed-form and numerical solutions for the probability distribution function of fracture diameters. *Int J Rock Mech Min Sci* 44(3):332–350. <https://doi.org/10.1016/j.ijrmmms.2006.07.013>
- Tonon F, Chen S (2010) On the existence, uniqueness and correctness of the fracture diameter distribution given the fracture trace length distribution. *Math Geosci* 42(4):401–412. <https://doi.org/10.1007/s11004-009-9228-2>
- Tuszynski J (2014) Surface Intersection. <https://www.mathworks.com/matlabcentral/fileexchange/48613-surface-intersection>. MATLAB Central File Exchange. Retrieved 30 June 2021
- Umili G, Bonetto SMR, Mosca P, Vagnon F, Ferrero AM (2020) In situ block size distribution aimed at the choice of the design block for rockfall barriers design: a case study along gardesana road. *Geosciences (switzerland)* 10(6):1–21. <https://doi.org/10.3390/geosciences10060223>
- Villaescusa E, Brown E (1992) Maximum likelihood estimation of joint size from trace length measurements. *Rock Mech Rock Eng* 25(2):67–87. <https://doi.org/10.1007/BF01040513>
- Vollgger SA, Cruden AR (2016) Mapping folds and fractures in basement and cover rocks using UAV photogrammetry, Cape Liptrap and Cape Paterson, Victoria, Australia. *J Struct Geol* 85:168–187. <https://doi.org/10.1016/j.jsg.2016.02.012>
- Wang X (2005) Stereological interpretation of rock fracture traces on borehole walls and other cylindrical surfaces. Faculty of the Virginia Polytechnic Institute and State University, 113. <http://scholar.lib.vt.edu/theses/available/etd-09262005-164731/>. Retrieved 15 August 2021
- Warburton P (1980a) A stereological interpretation of joint trace data. *Int J Rock Mech Min Sci Geomech* 17(4):181–190. [https://doi.org/10.1016/0148-9062\(80\)91084-0](https://doi.org/10.1016/0148-9062(80)91084-0)
- Warburton P (1980b) Stereological interpretation of joint trace data: influence of joint shape and implications for geological surveys. *Int J Rock Mech Min Sci Geomech Abstr* 17(6):305–316. [https://doi.org/10.1016/0148-9062\(80\)90513-6](https://doi.org/10.1016/0148-9062(80)90513-6)
- White C, Willis B (2000) A method to estimate length distributions from outcrop data. *Math Geol* 32(4):389–419
- Xu C, Dowd P (2010) A new computer code for discrete fracture network modelling. *Comput Geosci* 36(3):292–301. <https://doi.org/10.1016/j.cageo.2009.05.012>
- Zhang L, Einstein HH (1998) Estimating the mean trace length of rock discontinuities. *Rock Mech Rock Eng* 31(4):217–235. <https://doi.org/10.1007/s006030050022>
- Zhang L, Einstein HH (2000) Estimating the intensity of rock discontinuities. *Int J Rock Mech Min Sci* 37(5):819–837. [https://doi.org/10.1016/s1365-1609\(00\)00022-8](https://doi.org/10.1016/s1365-1609(00)00022-8)
- Zhang L, Einstein H, Dershowitz W (2002) Stereological relationship between trace length and size distribution of elliptical discontinuities. *Geotechnique* 6:419–433. <https://doi.org/10.1680/geot.2002.52.6.419>
- Zheng J, Deng J, Yang X, Wei J, Zheng H, Cui Y (2014) An improved Monte Carlo simulation method for discontinuity orientations based on Fisher distribution and its program implementation. *Comput Geotech* 61:266–276. <https://doi.org/10.1016/j.compgeo.2014.06.006>
- Zheng J, Deng J, Zhang G, Yang X (2015) Validation of monte carlo simulation for discontinuity locations in space. *Comput Geotech* 67:103–109. <https://doi.org/10.1016/j.compgeo.2015.02.016>
- Zheng J, Zhao Y, Lü Q, Liu T, Deng J, Chen R (2017) Estimation of the three-dimensional density of discontinuity systems based on one-dimensional measurements. *Int J Rock Mech Min Sci* 94(July 2016):1–9. <https://doi.org/10.1016/j.ijrmmms.2017.02.009>
- Zheng J, Guo J, Wang J, Sun H, Deng J, Lv Q (2022) A universal elliptical disc (UED) model to represent natural rock fractures. *Int J Min Sci Technol* 32(2):261–270. <https://doi.org/10.1016/j.ijmst.2021.12.001>
- Zou J, Hu X, Jiao YY, Chen W, Wang J, Shen LW, Gong S (2022) Dynamic mechanical behaviors of rock's joints quantified by repeated impact loading experiments with digital imagery. *Rock Mech Rock Eng*. <https://doi.org/10.1007/s00603-022-03004-5>

Publisher's Note Springer Nature remains neutral with regard to jurisdictional claims in published maps and institutional affiliations.